

# UVM ScholarWorks

## Numerical Study of Disperse Monopropellant Microslug Formation at a Cross Junction

Item Type	thesis;article
Authors	McDevit, Ryan
Download date	2026-05-13 01:12:16
Link to Item	<a href="https://hdl.handle.net/20.500.14849/3456">https://hdl.handle.net/20.500.14849/3456</a>

NUMERICAL STUDY OF DISPERSE MONOPROPELLANT MICROSLUG  
FORMATION AT A CROSS JUNCTION

A Thesis Presented

by

M. Ryan McDevitt

to

The Faculty of the Graduate College

of

The University of Vermont

In Partial Fulfillment of the Requirements  
for the Degree of Master of Science  
Specializing in Mechanical Engineering

October, 2011

# Abstract

Two immiscible fluids converging at microchannel cross-junction results in the formation of periodic, dispersed microslugs. This microslug formation phenomenon has been proposed as the basis for a fuel injection system in a novel, discrete monopellant microthruster design for use in next-generation nanosatellites. Previous experimental work has demonstrated the ability to repeatably generate fuel slugs with characteristics commensurate with the intended application. In this work, numerical modeling and simulation are used to further study this problem, and identify the sensitivity of the slug characteristics to key material properties including surface tension, contact angle and fuel viscosity. These concerns are of practical concern for this application due to the potential for thermal variations and/or fluid contamination during typical operation. For each of these properties, regions exist where the slug characteristics are essentially insensitive to property variations. Future microthruster system designs should target and incorporate these stable flow regions in their baseline operating conditions to maximize robustness of operation.

# Acknowledgements

First, and foremost, I would like to thank Professor Darren Hitt, whose support, guidance and patience made this work possible.

Special thanks to JW McCabe, who laid the groundwork for this thesis.

Funding for this work has been provided by NASA under Cooperative Agreement #NNX09A059

# Table of Contents

Acknowledgments .....	ii
List of Tables.....	vi
List of Figures.....	vii
<b>Chapter 1 Introduction.....</b>	<b>1</b>
1.1 Micro-Scale Propulsion . . . . .	4
1.2 MEMS-Based Thrusters . . . . .	6
1.2.1 MEMS-Based FEEP Thruster . . . . .	7
1.2.2 MEMS-Based Colloid Thruster . . . . .	8
1.2.3 Solid Propellant Digital Microthruster . . . . .	10
1.2.4 MEMS-Based Cold Gas Thruster . . . . .	11
1.2.5 Vaporizing Liquid Microthruster . . . . .	13
1.2.6 MEMS-Based Monopropellant Thruster . . . . .	14
1.3 Flow Actuation & Microvalves . . . . .	17
<b>Chapter 2 A Discrete Monopropellant Microthruster Concept .....</b>	<b>22</b>
2.1 Concept Overview . . . . .	24
2.2 Discrete Microslug Formation . . . . .	26

2.3	Preliminary Considerations . . . . .	29
<b>Chapter 3 Computational Methodology . . . . .</b>		<b>31</b>
3.1	Governing Equations . . . . .	31
3.1.1	Boundary Conditions . . . . .	34
3.2	Computational Implementation . . . . .	37
3.2.1	Baseline Material Properties . . . . .	37
3.2.2	2D vs. 3D Results . . . . .	37
3.2.3	Computational Domain & Grid Resolution Studies . . . . .	39
3.3	Experimental Setup . . . . .	42
3.4	Data Analysis . . . . .	44
3.4.1	Data Collection . . . . .	46
3.4.2	Slug Length Analysis . . . . .	47
3.4.3	Slug Volume Analysis . . . . .	48
3.4.4	List of Studies . . . . .	51
<b>Chapter 4 Results . . . . .</b>		<b>54</b>
4.1	Qualitative Comparison with Experimental Data . . . . .	54
4.2	Impact of Surface Tension Variation . . . . .	55
4.3	Impact of Contact Angle Variation . . . . .	61
4.4	Impact of Thermally-Induced Viscosity Variation . . . . .	63
4.5	Effective Impulse and Thrust . . . . .	67
<b>Chapter 5 Conclusions . . . . .</b>		<b>77</b>
5.1	Future Work . . . . .	78
<b>References . . . . .</b>		<b>80</b>

Appendix A ..... 85

# List of Tables

1.1	Parameters used in evaluation of microvalves . . . . .	18
1.2	Recent microvalve initiatives. Abbreviations are as follows, Style: NC = Normally Closed; Type: TP = Thermo-Pneumatic, BM = Bimorph, SMA = Shape Memory Alloy, ES = Electrostatic, PZ=Piezoelectric. . . . .	20
3.1	Properties of $H_2O_2$ and $N_2$ at STP . . . . .	37
3.2	Comparison of the initial slug in the “short” and “long” computational domains . . . . .	40
3.3	Comparison of relevant material properties used in the simulations and experiments . . . . .	43
3.4	Comparison of the different slug volume calculation methods . . . . .	50
3.5	Surface Tension Coefficient Studies . . . . .	52
3.6	Contact Angle Studies . . . . .	52
3.7	Fuel Viscosity Studies . . . . .	53

# List of Figures

1.1	Conceptual illustration of the ESA/NASA LISA mission. <i>Courtesy of NASA JPL website (<a href="http://lisa.jpl.nasa.gov">http://lisa.jpl.nasa.gov</a>)</i> . . . . .	5
1.2	Illustration of the Field Emission Electric Propulsion (FEEP) concept. Liquid metal propellant in the reservoir enters the slit via capillary action and exits at the accelerator. . . . .	8
1.3	Schematic representation of the FEEP thruster showing the etch and deposition required. Designed by Fleron [10] . . . . .	9
1.4	Basic operation of a colloid thruster using the electrospray technique. <i>Reproduced from Nabity [12]</i> . . . . .	9
1.5	Schematic of device built by Xiong <i>et al.</i> . The sandwich fabrication simplifies the etch geometry for each layer. Each layer is stacked and bonded to complete the thruster. Xiong <i>et al.</i> quotes several etch technologies including a KOH chemical etch and an inductively-coupled plasma etch. <i>Reproduced from Xiong [13]</i> . . . . .	10
1.6	Schematic of the sandwich constructed microthruster chip. The single-shot thrust concept was one popular among the aerospace community for its simple design and precise impulse bit. <i>Reproduced from Lewis [14]</i>	12

1.7	Digital solid propellant microthruster designed and built by TRW and Aerospace Corporation. <i>Courtesy of TRW. Reproduced from NASA GSFC Electric Eng. Div. website</i> . . . . .	13
1.8	Picture of the cold gas thruster presented by Fuqua <i>et al.</i> in 1999. The device is a sandwich design consisting of a propellant feed line, valve, plenum and nozzle. The device works properly during thruster operation. However leaks through the valve, which is common among cold gas thrusters, is an issue. <i>Reproduced from Fuqua [15]</i> . . . . .	14
1.9	VLM integrated with solenoid valve and Pyrex thermal standoff. <i>Reproduced from Blandino et al. [17]</i> . . . . .	15
1.10	VLM test model dimensions (top view, drawing not to scale): A=618 $\mu m$ , B= 62 $\mu m$ , C=709 $\mu m$ , D=7.8 mm, E=1.1 mm, and depth = 300 $\mu m$ . <i>Reproduced from Blandino et al. [17]</i> . . . . .	16
1.11	Illustration of the operation of a hydrogen peroxide thruster. <i>Reproduced from Hitt et al. [9]</i> . . . . .	16
1.12	A digital photograph of the completed MEMS diamond pillar microthruster. A top view is shown, with the inlet at the bottom and the nozzle at the top of the figure. To provide a reference length scale, a US penny is included in the background. <i>Reproduced from Hitt et al. [9]</i>	17
2.1	Image of the NASA/Goddard Space Flight Center prototype microthruster. . . . .	23

2.2	A schematic diagram depicting the envisioned operation of the discrete monopropellant thruster. Flows of a monopropellant and a gaseous inert fluid converge at a $90^\circ$ junction. The result is a periodic sequence of discrete monopropellant slugs, which propagate down the channel where they are chemically-decomposed in a catalytic bed. The energetic gases of decomposition in combination with the inert gas are then expanded in a converging/diverging supersonic nozzle to produce the target impulse for that slug. . . . .	25
2.3	An image of slug formation in a microchannel with the pressure at all inlets equal to 30 <i>psi</i> . . . . .	26
2.4	Photo of two phase flow structures in microchannels studied by Cubaud and Ho [22]. . . . .	27
2.5	Flow pattern map for a gasliquid flow in microchannels studied by Cubaud and Ho [23]. . . . .	28
3.1	Definition of the contact angle, $\theta$ within COMSOL. . . . .	36
3.2	Plots of the 3D simulation of the baseline case. . . . .	38
3.3	Comparison of the surface plots of the level set function for the 2D and 3D cases. . . . .	39
3.4	(a) The geometry of the microchannel used for flow visualization experiments. (b) The geometry of the computational domain that corresponds to the junction outlined in (a). . . . .	40
3.5	Plot of the slug length as a function of time for various grids. . . . .	42

3.6	a) Schematic of the microchannel chip layout. The insert shows the four-way junction. b) Schematic of the microchannel cross section. The width of the mask line is $10 \mu m$ . The top piece of glass has the access holes and the bottom piece has the etched pattern. The two are fused together in the final steps of the manufacturing process. . . . .	44
3.7	Layout schematic for the pressure supply system with locations of filters and measurement devices. . . . .	45
3.8	Sample surface plot of the baseline simulation. The liquid is represented in black, and the gas is represented in white. . . . .	46
3.9	Block diagram showing the general process of the MATLAB script. The outcomes are highlighted in orange. . . . .	46
4.1	A qualitative comparison of the experimental and numerical results. 1) The upstream attachment mechanism. 2) The downstream detachment mechanism. 3) The large, channel filling bubbles. . . . .	55
4.2	Sample of results generated by varying the surface tension coefficient with $\Delta V = 0$ over an equivalent time period, with the simulated monopropellant in blue. . . . .	56
4.3	A plot of slug length vs. surface tension coefficient for fixed $\Delta V = 0$ and $V_{liquid} = .4 \frac{m}{s}$ . . . . .	57
4.4	A plot of slug length vs. $\Delta V$ for three different surface tension coefficients. This plot highlights the similarity of the results. . . . .	58
4.5	A plot of slug formation frequency vs. surface tension coefficient, for $\Delta V = 0 \frac{m}{s}$ . There is a clear transition between $.06 \frac{N}{m}$ and $.07 \frac{N}{m}$ . . . . .	59
4.6	A plot of slug formation frequency vs $\Delta V$ for three different surface tension coefficients. This plot highlights the similarity of the results. . . . .	60

4.7	The plot of slug length as a function of contact angle. There is a clear transition between 155 and 160 degrees, which corresponds to a change in pinch-off mechanism. . . . .	62
4.8	Contour plots showing the change in detachment location that leads to change in microslug length. . . . .	63
4.9	A plot of slug length vs. $\Delta V$ for three different contact angles. This plot highlight the similarity of the results for these contact angles. . .	64
4.10	A plot of slug length vs. fuel viscosity for $\Delta V = 0$ . At 1.8 cP, the system transitions to annular flow, with no slugs being made. . . . .	66
4.11	A plot of slug formation frequency vs. fuel viscosity for $\Delta V = 0$ . As the system transitions to annular flow at 18 cP, the formation frequency drops to 0. . . . .	67
4.12	A plot of slug length vs. $\Delta V$ for two different fuel viscosities. There is a clear similarity between the two solutions. . . . .	68
4.13	A plot of slug formation frequency vs. $\Delta V$ for two different fuel viscosities. There is a clear similarity between the two solutions. . . . .	69
4.14	A plot of the total thrust vs. surface tension coefficient for $\Delta V = 0 \frac{m}{s}$ . The baseline thrust is plotted in green. . . . .	71
4.15	A plot of the impulse per slug vs. surface tension coefficient for $\Delta V = 0 \frac{m}{s}$ . . . . .	72
4.16	A plot of total thrust vs. contact angle for $\Delta V = 0 \frac{m}{s}$ . The baseline thrust is plotted in green. . . . .	73
4.17	A plot of impulse per slug vs. contact angle for $\Delta V = 0 \frac{m}{s}$ . . . . .	74
4.18	A plot of total thrust vs. viscosity for $\Delta V = 0 \frac{m}{s}$ . The baseline thrust is plotted in green. . . . .	75
4.19	A plot of impulse per slug vs. viscosity for $\Delta V = 0 \frac{m}{s}$ . . . . .	76

# Chapter 1

## Introduction

Recent initiatives in the satellite technology sector have shown the benefits of miniaturized satellites and point to the needs of future missions. Driven by the need to lower costs, lower post launch maintenance and increase reliability, miniaturized satellites are increasingly being used for a wide range of applications by academia, government and industry. One of the major initiatives to meet these goals is the focus on a group of miniaturized satellites ( $> 10kg$ ) called nanosatellites [1]. Nanosatellites, or “nanosats” allow for new science and communication missions by using satellite designs that would not be feasible, either from a design standpoint or due to budget constraints, with typical satellite architectures. Early efforts in nanosat design include the CubeSat program, which is a set of specifications for a  $10 \times 10 \times 10$  *cm* satellite that weighs  $1$  *kg* and is intended primarily for academic use. This system, designed by CalPoly and Stanford in 1999 [2] was created to be low cost ( $> \$40,000$ ) by using off-the-shelf components. Due to the small volume and mass limitations, CubeSats generally do not contain any thrusters on-board for precision station-keeping maneuvers. This limits their ability to perform precision communications or surveillance missions, as both of these require maintaining position and orientation for success.

As mission designers focus on replacing larger satellites with nanosats, or fleets of nanosats, developing appropriately-sized thrusters that are capable of Current NASA and DoD goals for future nanosats require thrusters which are capable of thrust levels and impulse bits on the order of (10-100  $\mu N$ ) and (100-1000  $\mu N \cdot s$ ) respectively [3].

To date no MEMS-based propulsion systems have been implemented in nanosatellites, however some have been flight tested for demonstration and experimental purposes. Most recently, the Electric Microthruster Test in Space (EMITS) was one such demonstration for flight testing a small-scale FEEP thruster capable of  $< 1\mu N$  thrust levels [4]. This device was launched aboard a Space Shuttle mission as part of the NASA Hitchhiker program using a Get-Away-Special (GAS) canister. FEEP, or Field Emission Electric Propulsion, is of great interest to the small spacecraft community because of its simplicity and thrust ranges. Typical thrust ranges are between 1 and 100  $\mu N$  for drag free control and as high as 1 mN for larger crafts, however the device itself is not a MEMS-based thruster but rather a MEMS-hybrid. The PRISMA program, which launched in early 2010 and is currently ongoing, is positioned to be the first flight demonstration of MEMS-based propulsion in a formation-flying test. The propulsion system for this mission, designed by NanoSpace, is a MEMS-based cold gas thruster with thrust output in the micro- to milli- Newton range. These propulsion system tests are the next step toward realizing some of the next generation science missions.

When speaking of micropropulsion systems, there is a distinction between micro-level thrusters, and micro-scale thrusters. While nanosats will require micro-scale propulsion systems, owing to their small size, there are missions currently in development that will use large ( $> 20$  kg) satellites that require micro-level thrust as part of their mission design. One such mission that requires micro-level thrust is the NASA/ESA LISA mission, or Laser Interferometer Space Antenna. LISA, which

is currently scheduled for an early 2012 launch, will study gravity waves, how they propagate and the sources that emit them, first postulated in Einsteins Theory of General Relativity. An illustration of the proposed design is shown in Figure 1.1. The antenna is made up of three identical drag-free<sup>1</sup> spacecraft arranged in a triangle and placed at Lagrange points, the center of which orbits the Sun at 1 AU, and located 20° behind the earth. Each arm of the triangle is approximately five million kilometers and is roughly equilateral (due to these large spacings one spacecraft has an orbit that intersects with the orbital path of Venus). The individual spacecraft will each require special heliocentric orbits to minimize the change in distance between them. The drag-free portion of the spacecraft is two test masses made of 75% gold and 25% platinum, highly polished to function as a mirror and in the shape of a cube. The test masses must maintain a central position in the craft to within a picometer. Laser light is emitted from one spacecraft toward each of the others and reflected off of the test mass to a sensor attached to the craft. The craft that receives the first beam emits an in-phase beam at that precise moment back to the original craft. This is done because of the decay in amplitude of the laser light over this large distance. In a sense the second craft serves as a laser light repeater. However, since the spacecraft are all identical either one may act as the initiator and therefore can conduct measurements concurrently. This provides redundancy to the system as well as adding to the accuracy in measurement [5]. In addition to the complexities of orbital flight dynamics associated with these requirements each spacecraft must be capable of minimizing orbital perturbations and attitude changes due to non-gravitational forces while keeping the test masses at the center of the spacecraft. Both radiation pressure

---

<sup>1</sup>A drag-free satellite is constructed of a freely floating object housed within an enclosed body or craft. The craft is typically chasing the freely floating object by firing thrusters mounted on its exterior attempting to keep the object in the center of the craft.

and solar wind can perturb the spacecraft on a magnitude equal or greater than that which the measurement can withstand. For example, radiation pressure due to solar activity is measured to be on the order of  $10^{-5} Pa$  at a distance of 1 AU from the Sun, the pancake-shaped craft is 2.7 m in diameter and weighs 575 kg [5]. In the simplest scenario the thrust,  $F_T$  required to cancel the force due to radiation pressure is roughly  $F_T = PA = (10^{-5} Pa)(\pi(2.7m)^2/4) = 57\mu N$ , which is within the quoted thrust expectation given in the previous section. In order to obtain an accuracy on the order of a picometer using this thrust level would require an impulse bit,  $I_t$ , again using a simplified one-dimensional case, of  $I_t = F_T \Delta t$  where  $\Delta t$  is the time duration given by,  $\Delta T = \sqrt{\frac{2\Delta x}{F/m}}$ . With  $\Delta x$  being the change in distance increment, the simplified one-dimensional total impulse is  $I_t = F_T \sqrt{\frac{2\Delta xm}{F_t}} = \sqrt{2F_T \Delta xm} = 4.5 \cdot 10^{-3} N \cdot s$ , again within the previously quoted values. In addition, the solar wind or plasma is composed of high velocity ions (400-700 km/s as measured by Mariner II) imparting an additional force on the craft [6]. These requirements are not capable of being met by traditional propulsion systems and with satellites decreasing in mass and footprint the best solution at present can be found in the emerging MEMS-based technologies. These devices will provide the necessary thrust and impulses with a compactness and redundancy never before seen in propulsion systems. In the next section some of the more prevalent MEMS-Based propulsion methods will be explored in more depth.

## 1.1 Micro-Scale Propulsion

Traditional thrusters used to perform station-keeping and orientation maneuvers have typically had masses, volumes and/or power consumption that would be too large for a nanosat. Attempts to miniaturize traditional systems, such as cold-gas thrusters, have been reported as early as 1992 [7], but this system suffered from propellant

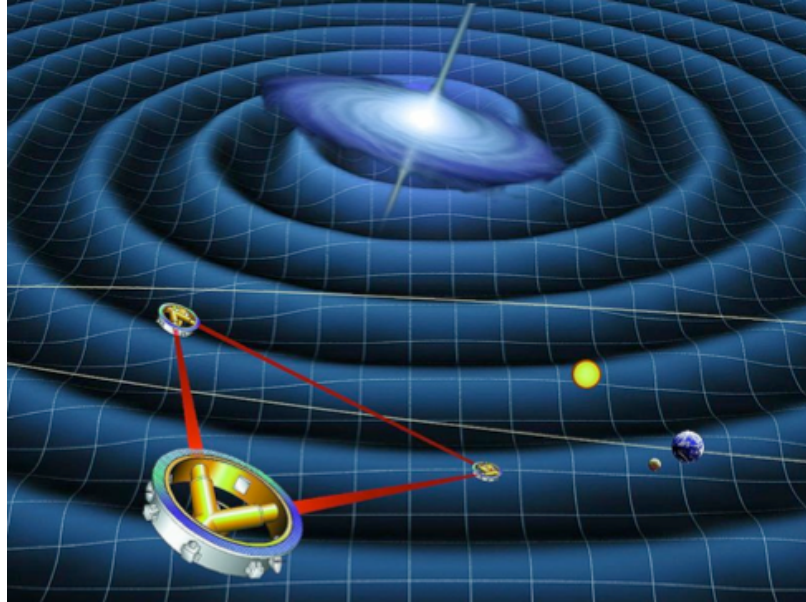


**Figure 1.1:** Conceptual illustration of the ESA/NASA LISA mission. *Courtesy of NASA JPL website (<http://lisa.jpl.nasa.gov>)*

leakage, and the need to store relatively large, high-pressure tanks to carry enough propellant for many missions. Electric propulsion, which is desirable for its high specific impulse ( $I_{sp}$ ), has so far been unable to scale down enough to be a practical micropropulsion option.

While these, and other, initiatives may ultimately be successful with further technological advances, the consensus among experts in the micropropulsion field is that the immediate future lies in MEMS<sup>2</sup>-based chemical thrusters due to their small size, relatively low cost and fully-integrated approach to on-board system architecture. Based on the techniques developed for semiconductor manufacturing, MEMS fabrication uses precision manufacturing techniques to miniaturize standard chemical thrusters to a scale suitable for nanosats. At the most basic level, a liquid chemical thruster can be broken into its core components: a propellant delivery system, a fuel-

---

<sup>2</sup>Micro-electro-mechanical System

injection system, a combustion chamber and a supersonic nozzle. Depending on the specific type of thruster these subsystems may be simple or quite complex. The goal of the MEMS approach is to shrink each of these components down and integrate them into a single system.

## 1.2 MEMS-Based Thrusters

As MEMS manufacturing is based on semiconductor fabrication techniques, it is unsurprising that they have followed a similar miniaturization path. Advances in materials science and processing techniques have allowed for increasingly complex systems that are orders of magnitude smaller than the first systems. Of particular interest for nanosat designers is the incorporation of MEMS technology into micropropulsion systems [1]. Most of these MEMS-based thrusters are miniaturizations of existing systems.

Most current MEMS manufacturing is done on silicon wafers, or ‘chips’, due to its semiconductor heritage. This imposes limits on the use of other materials that may be desirable, but thin film deposition techniques (silicon oxide, silicon nitride, etc.) have been developed that allow for the inclusion of other materials to be integrated during the manufacturing process. Additionally, new nanoscale manufacturing techniques, like nanorods made of various materials, show promise as catalysts in propellant decomposition in monopropellant thrusters.

The focus on MEMS-based micropropulsion initiatives began in the 1990’s, spearheaded by research at the Aerospace Corporation and NASA’s Jet Propulsion Laboratory (JPL) [1]. These early efforts were focused on electric propulsion, including resistojets, ion propulsion and FEEP thrusters. Later in the decade, focus turned to liquid thrusters such as the Vaporizing Liquid Microthruster (VLM) at JPL [8]

and more recently a MEMS-based monopropellant thruster using hydrogen peroxide decomposition [9]. In the following sections, these early efforts at MEMS-based thrusters will be discussed to highlight the challenges that exist for each technology.

### 1.2.1 MEMS-Based FEEP Thruster

Development of a MEMS-based FEEP thruster is an area of ongoing research; while there have been several FEEP thrusters used aboard spacecraft, such as the EMITS program, miniaturization has proven challenging. The underlying concept of a non-MEMS FEEP thruster is highlighted in Figure 1.2. A liquid metal, typically cesium, rubidium or indium is used as a propellant. The propellant is stored within the emitter module consisting of two metallic plates sandwiched together but electrically isolated from one another. The propellant flow enters the slit module by capillary action and the free surface at the slit exit is exposed to a strong electric field, on the order of  $10^9 V/m$ . The free surface undergoes a local instability due to the electrostatic forces and surface effects, resulting in Taylor cones. At the tip of these cones atoms spontaneously ionize at which point the accelerator electrode forces the ionized atoms to eject from the device. There is an electron build-up in the propellant storage reservoir that must be neutralized by electron emission into the ion jet.

To achieve this on the MEMS scale capillary tubes are etched using DRIE <sup>3</sup> into the handle wafer on an SOI <sup>4</sup> substrate. The slit is within the oxide layer and the accelerator and neutralizer modules are within the device layer of the SOI. In Figure 1.3 the cross section of a single device is shown. In the work done by Fleron and Hales [10] a matrix of these capillaries are etched into the SOI substrate and are sectioned into individually addressable areas to vary the thrust level. The work done by Fleron

---

<sup>3</sup>Deep Reactive Ion Etching

<sup>4</sup>Silicon-on-Insulator

as well as work done by Scharlemann [11] on the In-FEEP project is some of the most recent in MEMS-based FEEP technology.

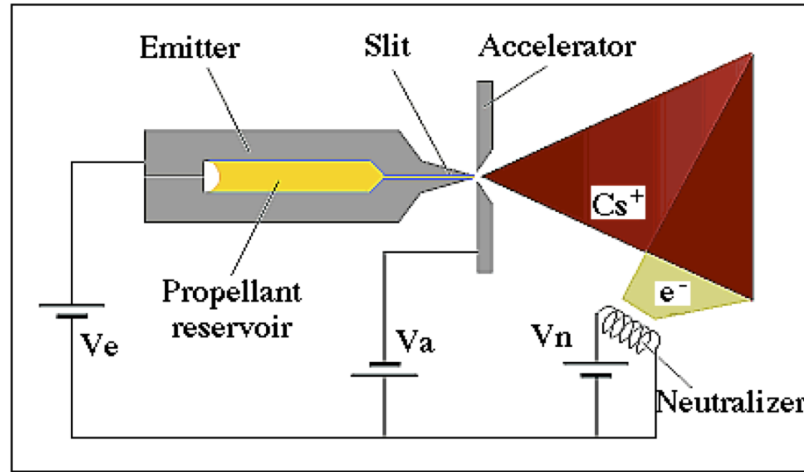


**Figure 1.2:** Illustration of the Field Emission Electric Propulsion (FEEP) concept. Liquid metal propellant in the reservoir enters the slit via capillary action and exits at the accelerator.

### 1.2.2 MEMS-Based Colloid Thruster

Similar, but slightly different in terms of the physics, the MEMS-based colloid thruster is another popular EP concept. Shown below in Figure 1.4 the colloid thruster employs a liquid propellant electro spray scheme to generate thrust.

High charge-to-mass ratio liquid (formamide or tributyl phosphate were studied by Nabity *et al.* [12]) is stored in a propellant reservoir usually on the chip. By capillary action the liquid flows into the emitter and exits in a steady stream of micro-droplets by the classical Rayleigh break-up mechanism. The charged droplets are then accelerated through the extractor module at high velocities thereby generating thrust. The ion emission exploited by the FEEP thruster may also occur here depending on the strength of the electric field during acceleration as well as the charge associated with the droplets. Nabity *et al.* mention that this may be advantageous

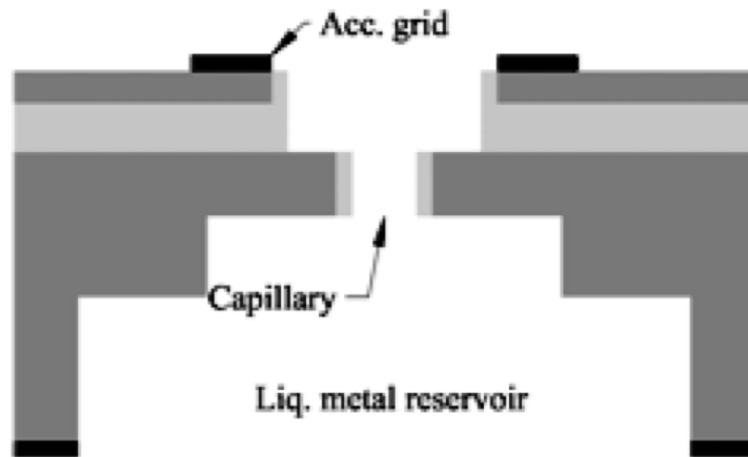


**Figure 1.3:** Schematic representation of the FEEP thruster showing the etch and deposition required. Designed by Fleron [10]

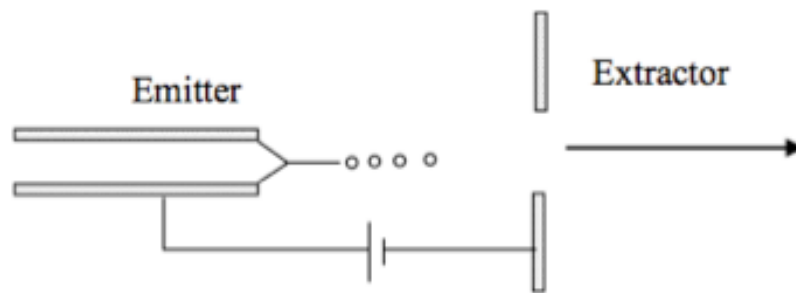


**Figure 1.4:** Basic operation of a colloid thruster using the electro spray technique. *Reproduced from Nabity [12]*

for increasing the specific impulse due to ions having a much greater charge-to-mass ratio, however this will decrease mass flow rate and consequently decrease the output thrust. Also, the liquid must have a low vapor pressure to avoid a phase change where it is not intended. These special requirements on propellant has led to much research into so-called ionic liquids. These liquids, when combined with low vapor pressure solvents, create mixtures that are custom tailored to the propulsion requirements of the particular mission.

While the colloid thruster was thoroughly examined in the 1960's and 1970's the

relatively large starting and working voltages [12] have limited its application. The range, 5 - 10 kV, creates a rather serious packaging problem for use onboard nanosats [13]. However, the recent MEMS technological advances has allowed for a decrease in startup voltages down to 1400 V [13]. The schematic of the device built by Xiong *et al.* is shown in Figure 1.5.

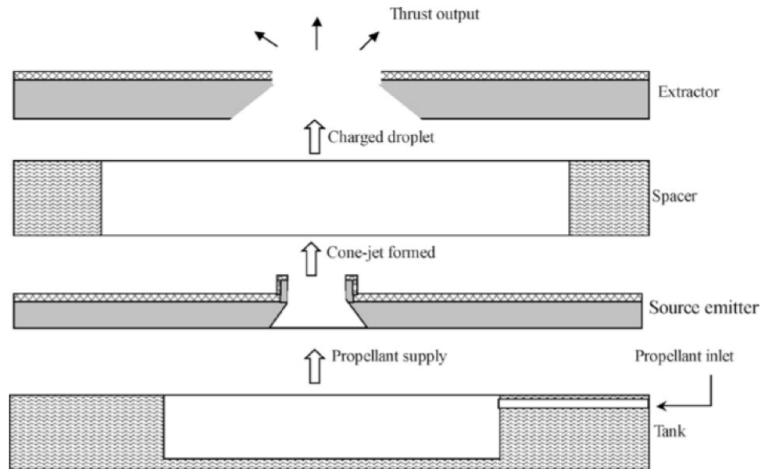


**Figure 1.5:** Schematic of device built by Xiong *et al.*. The sandwich fabrication simplifies the etch geometry for each layer. Each layer is stacked and bonded to complete the thruster. Xiong *et al.* quotes several etch technologies including a KOH chemical etch and an inductively-coupled plasma etch. *Reproduced from Xiong [13]*

Currently, the major challenges to the thruster development are the ability to miniaturize high performance extraction electrodes with a large array of emitters. The degradation of the potential field along the array will produce inconsistent thrust levels [12].

### 1.2.3 Solid Propellant Digital Microthruster

Around the end of the 1990's digital micropropulsion using solid propellants gained popularity in the aerospace industry. TRW, The Aerospace Corp. and Caltech under

Lewis *et al.* [14] began the Digital Propulsion project in the hopes of offering new orbit and station-keeping operations at a fraction of the current costs. The schematic of the device designed by Lewis *et al.* is shown in Figure 1.6.

The design consists of three silicon wafers, each containing a module of the thruster, sandwiched together. The impulse bit is defined within the middle die. The type of propellant and the size of each plenum may be changed depending on the impulse bits needed for a particular mission. The top die consists of two components, a diaphragm layer in contact with the middle die, which serves as a burst disk for each plenum and an array of expansion nozzles. The igniters are resistor elements fabricated on the bottom die. When ignited the pressure in the plenum increases until the burst pressure of the diaphragm layer is exceeded. The expansion nozzle helps to convert the thermal energy into thrust. A fully assembled digital microthruster chip is shown in Figure 1.7.

The limitations in this device are readily apparent, most notably the thruster has a predetermined number of firings available. However, the digital propulsion concept may be useful in the design of a chemical propulsion thruster. As will be discussed in Chapter 2, advances in the field of microfluidics may shine new light on this novel concept.

#### **1.2.4 MEMS-Based Cold Gas Thruster**

A cold gas microthruster is probably the simplest in design of all the MEMS-based propulsion concepts. It consists of a propellant tank or reservoir, a nozzle plenum, a microvalve, and a supersonic micronozzle. In operation, the propellant flows from the storage tank into a nozzle plenum, which serves as the constant pressure source for the supersonic nozzle. The flow is then accelerated as it enters a micron-size De

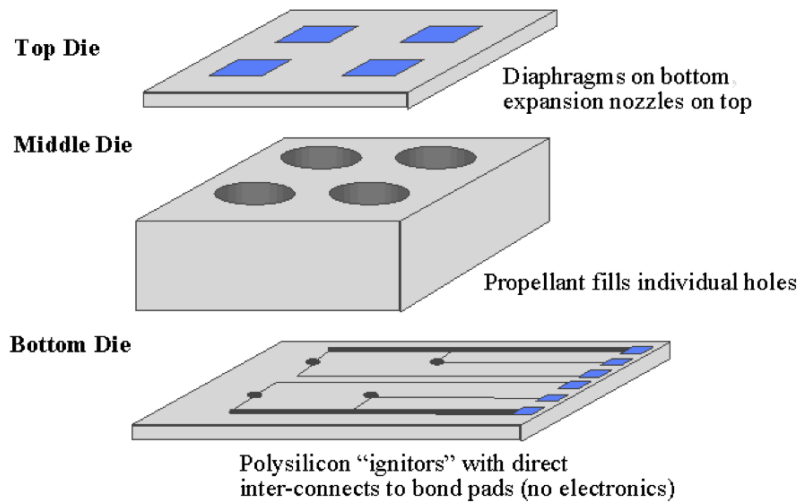


**Figure 1.6:** Schematic of the sandwich constructed microthruster chip. The single-shot thrust concept was one popular among the aerospace community for its simple design and precise impulse bit. *Reproduced from Lewis [14]*

Laval nozzle or micronozzle. The micronozzle is an essential component of the device and requires a specific geometry to generate the target thrust level. One of the first miniature cold gas thrusters was designed by Fuqua *et al.* [15]. Their design is shown in Figure 1.8.

As with all chemical MEMS-based microthrusters this miniaturization comes at a cost. The surface area-to-volume ratio increases dramatically compared with traditional thrusters designed for large satellites. This increases the viscous losses and attributes to design concerns due to boundary layers being on the same order of magnitude as the nozzle geometry. However, micronozzles allow the system to be run at a much higher pressure than traditional thrusters and can overcome the viscous losses while still providing the low thrust levels required [16]. It is worth noting here that the cold gas thruster encompasses the bare-bones system of any supersonic chemical microthruster design.

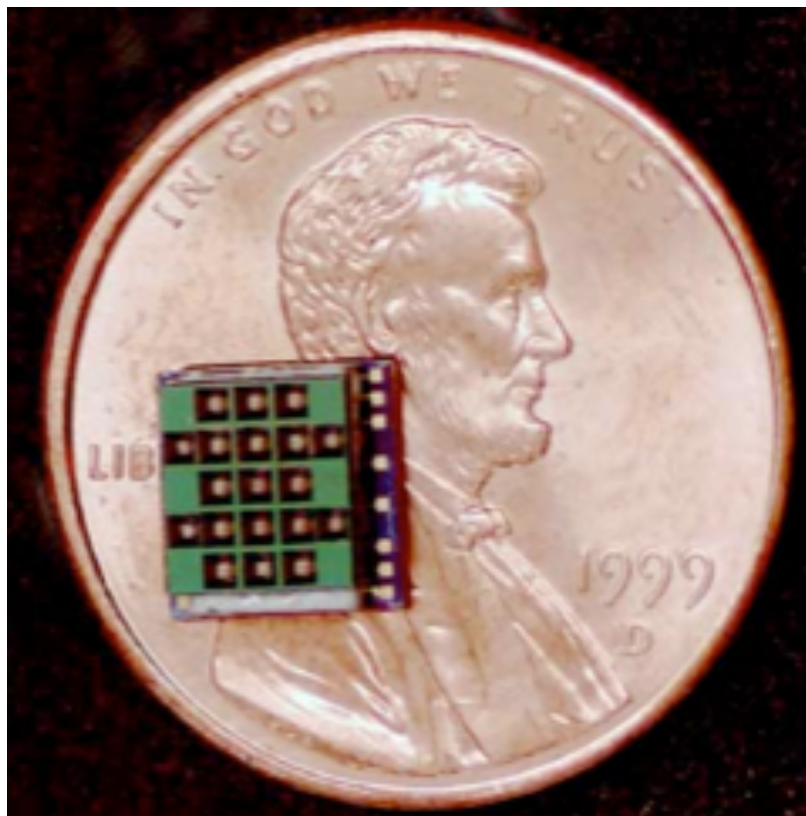


**Figure 1.7:** Digital solid propellant microthruster designed and built by TRW and Aerospace Corporation. *Courtesy of TRW. Reproduced from NASA GSFC Electric Eng. Div. website*

### 1.2.5 Vaporizing Liquid Microthruster

The vaporizing liquid microthruster (VLM) developed at the JPL represents another possible candidate for attitude control of microspacecraft. The VLM is an electrothermal thruster in which a liquid propellant is heated to vaporization and expelled through a nozzle to produce thrust. The VLM is intended to produce thrust in the range of 0.1-1.0 mN and have a minimum impulse bit capability of  $10^{-7}$  to  $10^{-5} N \cdot s$ . In this role, the specific impulse is not as critical a driver as would be the case for a primary propulsion system [17]. Tests to date have focused on water as a propellant although others that have been considered include ammonia and

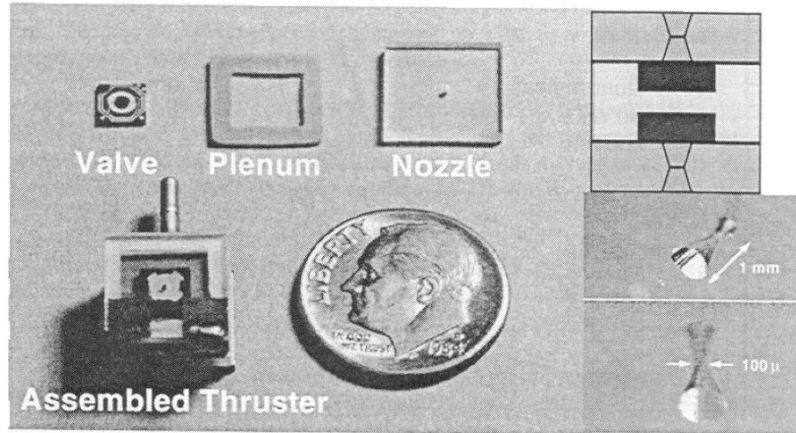


**Figure 1.8:** Picture of the cold gas thruster presented by Fuqua *et al.* in 1999. The device is a sandwich design consisting of a propellant feed line, valve, plenum and nozzle. The device works properly during thruster operation. However leaks through the valve, which is common among cold gas thrusters, is an issue. *Reproduced from Fuqua [15]*

hydrazine.

The VLM is fabricated using MEMS techniques, which have made it a candidate for some microspacecraft designs with very limited surface area available for installation. In the most recently tested versions of the VLM, a compact (but not MEMS fabricated) valve is mounted to a Pyrex thermal standoff just upstream of the heater channel inlet as shown in Figure 1.9. The propellant supply capillary runs through this standoff.

While the VLM offers promise for future use, it is currently limited by the amount of power required to phase change the propellant. As the power generation equipment improves, the VLM may become a candidate for future missions.

### 1.2.6 MEMS-Based Monopropellant Thruster

A second type of liquid propellant thruster that has been proposed is a MEMS-based monopropellant thruster. In Hitt *et al.* [9] a thruster based on catalyzed hydro-

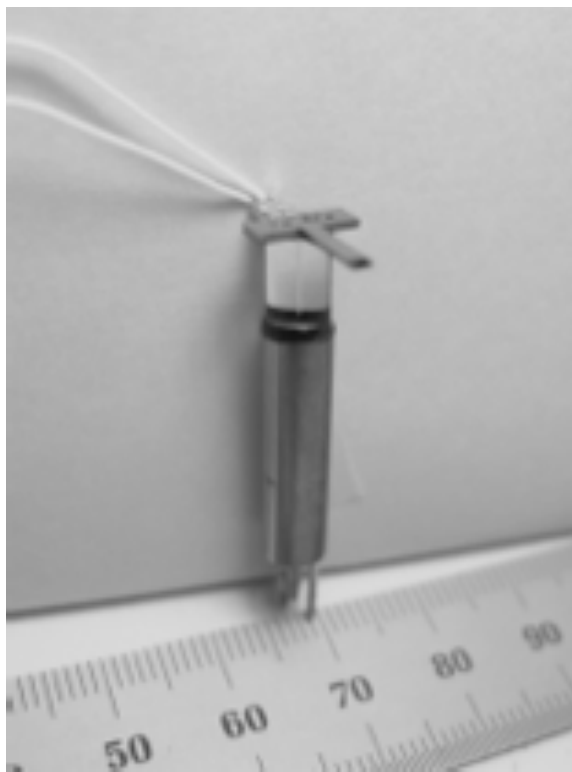


**Figure 1.9:** VLM integrated with solenoid valve and Pyrex thermal standoff. *Reproduced from Blandino et al. [17]*

gen peroxide decomposition was described. This system works on principles similar to macro scale hydrogen peroxide thrusters; the general operation is highlighted in Figure 1.11.

In a prototype developed at NASA Goddard Space Flight Center in collaboration with the University of Vermont, the plenum, injection system, catalytic chamber and supersonic nozzle are all integrated into the package. For scale, the thruster is shown next to a US penny in Figure 1.12.

In Hitt *et al.*[9] one aspect of the design which was highlighted for further improvement was the microvalve that controls the propellant flow. The operation of a micro-thruster consists of the delivery of a specified amount of impulse to the spacecraft and is thus inherently transient in nature. For a monopropellant thruster this

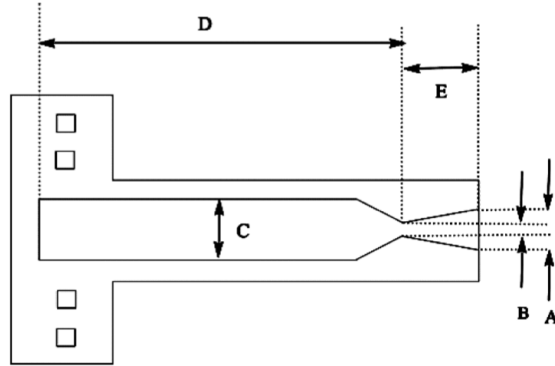


**Figure 1.10:** VLM test model dimensions (top view, drawing not to scale):  $A=618 \mu m$ ,  $B= 62 \mu m$ ,  $C=709 \mu m$ ,  $D=7.8 \text{ mm}$ ,  $E=1.1 \text{ mm}$ , and depth =  $300 \mu m$ . *Reproduced from Blandino et al. [17]*

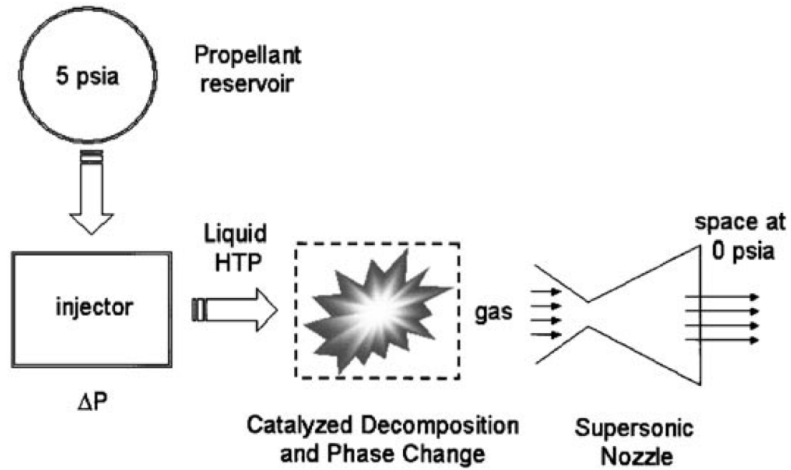


**Figure 1.11:** Illustration of the operation of a hydrogen peroxide thruster. *Reproduced from Hitt et al. [9]*

involves the throttling of the propellant via a microvalve. The limiting resolution for thrust and impulse delivery to the nanosat is thus intimately linked with the ability to precisely actuate the microvalve.



**Figure 1.12:** A digital photograph of the completed MEMS diamond pillar microthruster. A top view is shown, with the inlet at the bottom and the nozzle at the top of the figure. To provide a reference length scale, a US penny is included in the background. *Reproduced from Hitt et al. [9]*

### 1.3 Flow Actuation & Microvalves

Interest in MEMS-based microvalves spans multiple disciplines with most recent research conducted within the semiconductor processing, automotive, genetics and micropropulsion communities. The purpose of the valve is generally the same, to allow very small volumes of fluid to be accurately controlled within the microfluidic system. As on the macro-scale MEMS-based microfluidic system will be required to isolate and regulate flows. This is typically done with isolation-type (i.e. check, ball, gate, etc.) valves and pressure regulating valves. Subcomponents of these valves include springs, steel balls, metal diaphragms, solenoids, pneumatics, etc. all of which do not lend themselves to simple macro-to-MEMS conversion and integration.

Furthermore, micropropulsion inspired microvalves must meet the challenges of the applicable space environment as well as the limited power available onboard nanosats. The generally accepted power value in current nanosat concepts is  $< 20$

**Table 1.1:** Parameters used in evaluation of microvalves

---

Size and Weight	Power Consumption
Voltage	Minimum Valve Cycle Time
Pressure Requirements	Leakage
Liquid Propellant Compatibility	Valve Seating Force
Filtration	

---

W with maximum bus voltages of 15 V, with 5 V being the target for future designs [18]. This restriction has caused the reemergence of MEMS-based chemical propulsion as the choice micropropulsion system for microspacecraft since the power usage is limited to valve actuation and control electronics.

Implementation, however, is dependent on the advancement of microvalve technology from its current state. Final assembly of a MEMS-based chemical propulsion system must include valves and, to date, microfabrication of microvalves via MEMS techniques has proved challenging. It may be possible to design a MEMS-based chemical propulsion system with only external valves, but this will inevitably lead to larger impulse bits.

In Mueller’s review of the state of microvalve technology [18], he lists a set of nine metrics that microvalves may be evaluated on, shown in Table 1.1. This list was generated for shutoff valves that are intended to be cycled many times, as opposed to a single-use valve also known as a micro-isolation valve.

Of particular interest here is the minimum valve cycle time, leakage and pressure, all others on the list would be considered prerequisites for micropropulsion consideration for nanosats. The flow rate due to leakage must be small enough as to produce a negligible amount of thrust for a given mission profile. If this leakage thrust is

too large the propulsion control system would be continuously thrusting in order to stabilize the position/orientation of the craft. In addition, a large leakage rate would require a larger initial propellant mass. Both issues compound the inefficient use of the propellant and as a result undermine the minimization of overall system mass.

Pressure requirements are generally dependent on the power consumption, materials, geometry and the dynamics involved in valve operation. The majority of microvalves have maximum inlet pressures on the order of 100 *psi*, with some < 10 *psi*. The maximum inlet pressure is a function of the power consumption and voltage in conjunction with the valve geometry. An increase in inlet pressure will, in general, require an increase in electrical power to open the valve. Mueller also notes that a normally-closed valve design should only be considered due to the continuous power consumption required to operate a normally-open design and if a power failure were to take place the thruster would continue to fire. As mentioned in the beginning of this chapter the minimum impulse bit of a micropropulsion system will determine its applicability for a given mission. The thrust and the minimum valve cycle time will define the minimum impulse bit as:

$$I_{bit} = \int_{t_{on}}^{t_{off}} F(t)dt \quad (1.1)$$

The thrust,  $F(t)$ , will not be constant throughout the operation of the valve. The transient thrust force during the opening and closing of the valve must be examined to properly determine the minimum impulse bit. The ideal microvalve would have a response time of less than 10 *ms*, be capable of handling pressures at least as high as 100 *psi* and leakage rates that would produce thrust levels several orders of magnitude less than the target thrust. Table 1.2 provides the data for several microvalves currently in production or development. The data was collected from several papers including Mueller's review as well as a review by Oh *et al.* [19].

**Table 1.2:** Recent microvalve initiatives. Abbreviations are as follows, Style: NC = Normally Closed; Type: TP = Thermo-Pneumatic, BM = Bimorph, SMA = Shape Memory Alloy, ES = Electrostatic, PZ=Piezoelectric.

Microvalve			Parameters		
Owner/Author	Type	Style	Response Time (ms)	Applied Pressure (psi)	Power (W)
Redwood	TP	NC	400	100	2
HP	BM	NC	100	200	1
IC Sensors	BM	NC	100	50	.5
TiNi Co.	SMA	NC	21	400	2
MIT/Bosch	ES	NC	N/A	60	200 V
JPL	PZ	NC	.1	50	.004

This table, composed of a sample of valves, shows that microvalve technology can satisfy some metrics but is not yet appropriate for propulsion flow control in a space environment.

Unfortunately, flow control in micro-valves remains a prominent challenge within the field of microfluidics; indeed, the limited precision in valve actuation is such that the associated residual impulse may exceed twice the design impulse resolution. Given the inherent throttling limitations and errors, it is important to investigate alternative methods for achieving the needed level of flow control.

One possible solution is to deliver the monopropellant to the thruster in discrete quantities rather than as a continuous stream. This principle has been previously demonstrated for solid propellants in the DARPA ‘digital microthruster’. In previous experimental work at the University of Vermont, McCabe *et al.*[20] demonstrated the ability to repeatably generate discrete fuel ‘slugs’ appropriate to micro-propulsion applications using converging liquid and gas flows at a microchannel junction. Provided that the discrete monopropellant slugs each produce an impulse well below the design

resolution, then a target level of impulse can be delivered to the nanosat by allowing the passage of a finite number of slugs through the valve. In essence, the slug formation process represents a virtual self-valving mechanism which affords finer resolution than a micro-valve for a continuous stream. McCabe *et al.*[20] demonstrated that the slug size and frequency could be varied over a sizable range by carefully regulating inlet pressure conditions. Details of this micropropulsion concept are more fully described in Chapter 2.

The present study is intended to both complement and extend the work of McCabe *et al.* by developing a computational model capable of simulating the slug formation process. This numerical capability is significant in that it allows for sensitivity studies to be performed that are not easily accomplished experimentally: namely, the impact of variations in key gas/liquid properties (surface tension, contact angle, viscosity) that could potentially arise during an extended space mission due to fouling or thermal variations within the propulsion system.

## Chapter 2

# A Discrete Monopropellant Microthruster Concept

As highlighted in Chapter 1, monopropellant propulsion is an attractive scheme for microthruster applications due to its advantages over other propulsion types:

- Lower power requirements than electro-thermal and electric propulsion devices
- Higher propellant density and higher specific impulse than cold-gas thrusters
- Greater thrust and impulse bit control than solid propellant systems
- Simpler to design and operate than bipropellant systems

Monopropellant thrusters typically rely upon a catalyzed chemical decomposition of the liquid propellant as the source of energy. The chemical reaction, which is exothermic, produces a high-energy gaseous product, which is accelerated through a converging-diverging nozzle to generate thrust. Opening and closing the valve that controls the flow of the liquid propellant can control the impulse bit of the system. The first prototype monopropellant microthruster reported in literature was developed

at the NASA Goddard Space Flight Center in conjunction with the University of Vermont [9]. An SEM image of the prototype is shown in Figure 2.1.

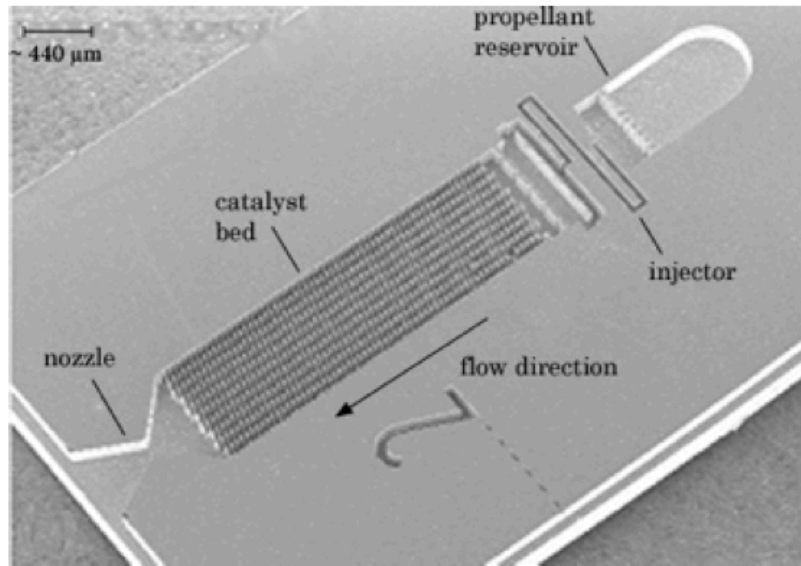
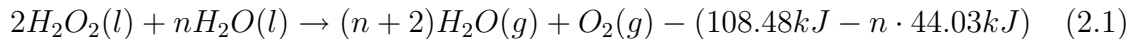


**Figure 2.1:** Image of the NASA/Goddard Space Flight Center prototype micro thruster.

This operation of this thruster is conceptually simple: a small amount of propellant is delivered to the catalytic bed where it decomposes. For this thruster, the monopropellant is High-Test hydrogen peroxide (HTP). The decomposition reaction is given by Equation 2.1, where  $n$  is the number of moles of  $H_2O$  for every two moles of  $H_2O_2$ . Propellant grade HTP is typically between 80% and 95%  $H_2O_2$  by volume.



As shown on the product side of the reaction, this reaction is highly exothermic, which causes the products to exit the catalytic bed at an elevated temperature and pressure. The quasi-2D nozzle converts this thermal energy into kinetic energy, which results in thrust for the system. In this design, the microvalve has two main purposes: to serve as a throttle on the amount of propellant entering the system, and to prevent

back flow after the thruster has been “shut-down”. The primary parameter that determines the effectiveness of a microvalve at throttling the flow is the response time. As discussed in Chapter 1, microvalves are an area of ongoing research but current designs lack the response time necessary to meet the (100-1000  $\mu N \cdot s$ ) impulse-bit requirements that NASA and the DoD have laid out. A limiting factor, then, in the use of monopropellant thrusters is the response time of the microvalves used in the fuel-injection system. In work by McCabe *et al.* [20] a microfluidic phenomenon, which results in the creation of discrete, monodisperse droplets, was proposed and studied as the basis of a fuel-injection system.

## 2.1 Concept Overview

Similar to the DARPA digital solid propellant microthruster, this design attempts to create a digital effect using a liquid monopropellant and an inert gas. A schematic demonstrating this concept is shown in Figure 2.2. Recent studies in the microfluidics literature have demonstrated that two immiscible liquids at a microscopic T-junction can be used to create slug structures that are periodic and highly repeatable.[21]. While these studies provide a foundation for further research they are limited in practical application due to the need to carry a second pressurized liquid on the satellite. The efficiency of the catalytic process in generating thermal energy may also be decreased due to the need to heat the inert fluid. In addition, if the secondary fluid is an oil, fouling will occur in the catalyst bed. Work has been performed by Cubaud *et al.* [22],[23] for gas-liquid flows in larger microchannels  $O[100\mu m]$ . These microchannels are too large for the intended microthruster application, and since the effects of surface tension will increase with decreasing channel size, smaller channels may exhibit different behaviors. In McCabe *et al.* [20], a pressure-driven system

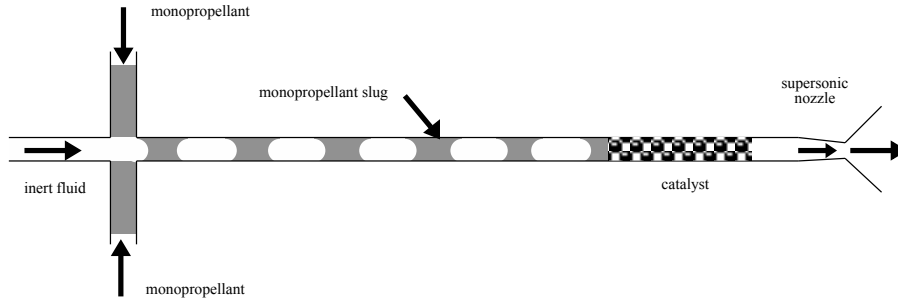


**Figure 2.2:** A schematic diagram depicting the envisioned operation of the discrete monopropellant thruster. Flows of a monopropellant and a gaseous inert fluid converge at a  $90^\circ$  junction. The result is a periodic sequence of discrete monopropellant slugs, which propagate down the channel where they are chemically-decomposed in a catalytic bed. The energetic gases of decomposition in combination with the inert gas are then expanded in a converging/diverging supersonic nozzle to produce the target impulse for that slug.

which was an order of magnitude smaller than that described in Cubaud *et al.* [23], was created to characterize the microslug formation by the inlet pressure ratio. They found that controlling the pressure ratio at the inlets allowed them to create steady, periodic microsugs of different sizes and lengths.

This microfluidic technique could be used to produce the ‘digital propulsion’ effect with a liquid monopropellant and inert gas. In this process, the liquid monopropellant and a second immiscible inert gas converge at a microscopic junction. The array of monopropellant slugs formed will flow through the outlet channel where they undergo a chemical decomposition in an *in situ* catalyst bed. This will be embedded directly into the channel thereby simplifying the geometry as well as decreasing the footprint on the chip. The inert fluid will pass through the bed chemically unaffected. The decomposition products then flow directly into a supersonic nozzle to convert the thermal energy into kinetic energy. By making the impulse bits sufficiently small,

a target impulse can be delivered with the passage of a set number of slugs, which effectively increases the resolution of the valve timing. While conceptually straightforward, the actual operation will depend principally upon the characteristics of the monopropellant slugs, which are formed. As monodisperse slug formation is a well-studied microfluidic process, an examination of the current state of research on the topic is useful.

## 2.2 Discrete Microslug Formation

The microslug flow pattern is essentially a droplet formation process occurring within a tube, pipe, or in this case a channel. Early studies, which focused on water-oil systems, demonstrated that when two immiscible liquids converge at a 3-way T-junction, a range of flow patterns can be created. An example of this slug-formation process is shown in Figure 2.3.

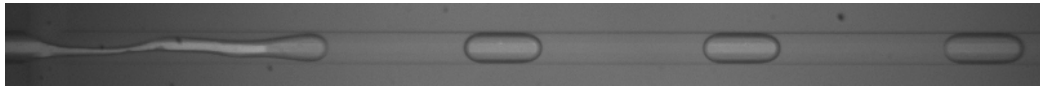


**Figure 2.3:** An image of slug formation in a microchannel with the pressure at all inlets equal to 30 *psi*.

Figure 2.4 is a series of photographs showing the different two-phase flow structures observed in microchannels. From the first photo in the series to the last mass flow rate of gas is increased. The observed patterns begin with bubbly flow where the gas bubbles are generally smaller than the channel width. Increasing the gas flow rate transitions the flow to a wedging structure and then to slug flow. The microthruster concept is intended to work in this slug flow region, as the distinct separation between the inert gas and the monopropellant will allow for discrete slugs. Controlling the size of these discrete slugs will allow for control over the impulse bit, which is the

primary goal of the fuel injection system.

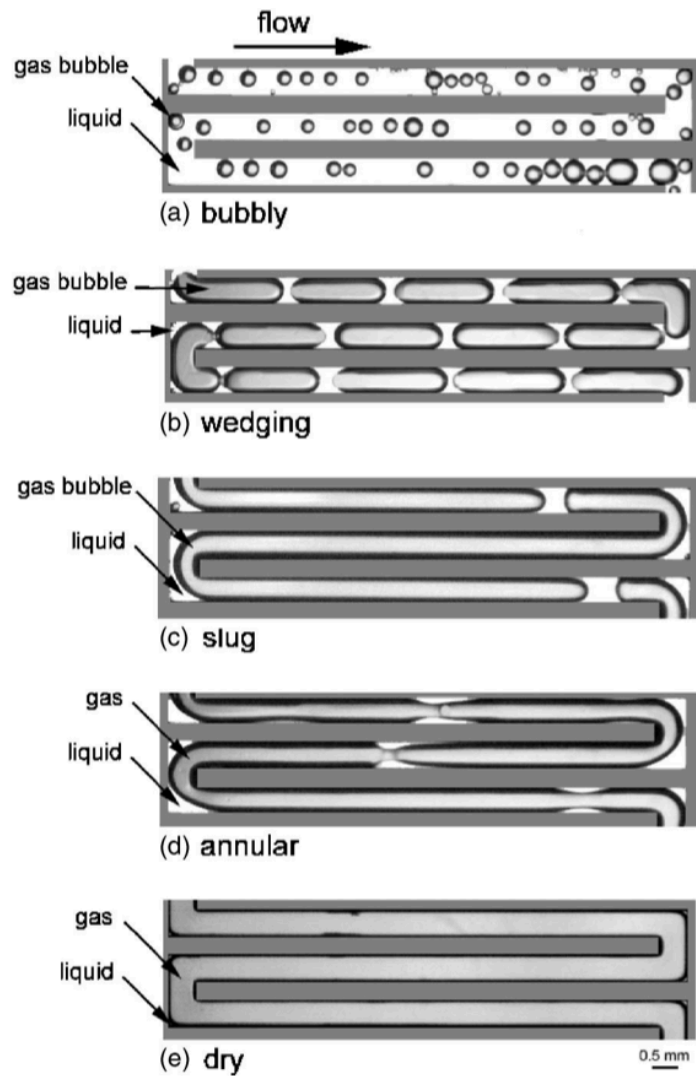


**Figure 2.4:** Photo of two phase flow structures in microchannels studied by Cubaud and Ho [22].

While this oil-water system is capable of creating the slug flow pattern, that is desired for this application, the need to carry the oil on the spacecraft, as well as the likelihood that the oil will foul the catalyst bed, make it an undesirable solution. Work by Cubaud *et al.* on gas-liquid flow patterns in a 4-way  $90^\circ$  junction demonstrated

that a similar range of flow patterns can be created using air and water. A two-phase flow map, shown in Figure 2.5, demonstrates that there is a similar slug flow region that exists for the gas-liquid system.

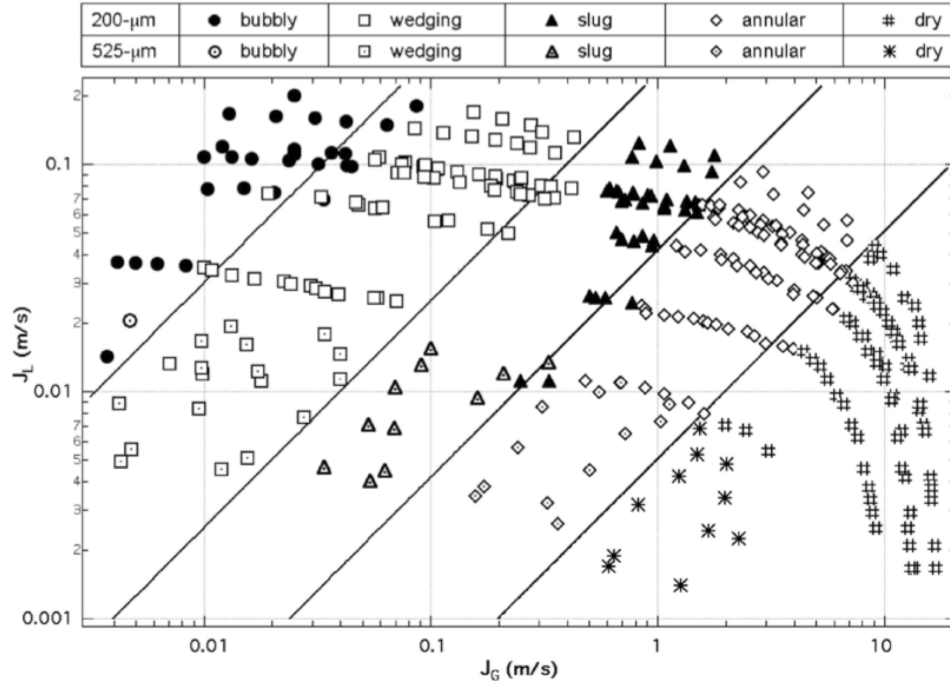


**Figure 2.5:** Flow pattern map for a gasliquid flow in microchannels studied by Cubaud and Ho [23].

In 2009, a microfluidic system was developed to study the feasibility of the ‘digital’ microfluidic fuel-injection scheme for a MEMS-based monopropellant microthruster by McCabe *et al.*[20]. Using an air-water system similar to that of Cubaud *et al.*, McCabe demonstrated that by lowering the air pressure, relative to the water pressure, and thus lowering the inlet velocity of the air, he could create a range of slug sizes within the slug forming regime. These results were promising, as they demonstrated that the fuel-injection system was capable of bringing the theoretical thrust and impulse bit into the range specified by NASA and the DoD.

## 2.3 Preliminary Considerations

In this work the slug flow pattern is dissected into two measurable quantities, namely pinch-off frequency,  $f$ , and slug length,  $L_s$ . These two variables characterize the flow and can be used to calculate both thrust and impulse bit. The pinch-off mechanism is commonly understood to be the competition between pressure and surface tension, as well as geometry and wall surface attributes such as contact angle. This process results in the periodic formation of monodisperse micro-slugs. Given some geometry, wall material(s) and fluid properties this can be written as:

$$f = g_1(\Delta P, P_{base}, \sigma, \theta, \mu, D_h, A) \quad (2.2)$$

$$L_s = g_2(\Delta P, P_{base}, \sigma, \theta, \mu, D_h, A) \quad (2.3)$$

where  $\Delta P$  is the difference in gas and liquid inlet pressures,  $P_{base}$  is the baseline inlet pressure of the liquid,  $\sigma$  is the surface tension,  $\theta$  is the contact angle,  $\mu$  is the dynamic viscosity of the liquid,  $D_h$  is the hydraulic diameter and  $A$  is the cross sectional area of the microchannel. A change in the baseline pressure will have an effect on the mean velocity of the flow. This term will account for the overall increase in mass flow rate.

Of the terms in each of these groups, the first two ( $\Delta P$  and  $P_{base}$ ) are the parameters that will be controlled to specify the flow and the last two ( $D_h$  and  $A$ ) are geometric parameters that are specified by the system. In contrast, the surface tension, contact angle and viscosity terms may vary during operation. One of the main conclusions of McCabe [24] was that surface tension effects dominate the slug formation process in smaller microchannels. Surface tension is a highly sensitive quantity that can be significantly affected by the presence of contaminants and variations in

temperature. Viscosity, another temperature-dependent material property, and contact angle, another property that could be affected by the presence of contaminants, are also parameters of interest. The goal of this study is to use computer simulations to examine the effects of these parameters on the slug formation process in the slug forming regime that was studied experimentally by McCabe.

# Chapter 3

## Computational Methodology

In Chapter 2, the relevant parameters of interest for the multiphase flow were found to be surface tension coefficient ( $\sigma$ ), contact angle ( $\theta$ ) and dynamic viscosity of the monopropellant ( $\mu$ ). The goal of this study was to determine the impact of each of these parameters on the operation of the proposed microthruster. To achieve this goal, computational fluid dynamics (CFD) simulations were performed, including a formulation for tracking the interface between the two phases. In section 3.1, the mathematical formulation of the transport equations will be presented, and in section 3.2 the computational methods used to solve these equations will be presented.

### 3.1 Governing Equations

In this study, the unsteady, incompressible Navier-Stokes equations were solved:

$$\nabla \cdot \mathbf{u}_i = 0 \quad (3.1)$$

$$\rho_i \frac{\partial \mathbf{u}_i}{\partial t} + \rho_i (\mathbf{u}_i \cdot \nabla) \mathbf{u}_i = \nabla \cdot [-p\mathbf{I} + \mu_i (\nabla \mathbf{u}_i + \nabla \mathbf{u}_i^T)] + \vec{F}_{ST} \quad (3.2)$$

where  $\mathbf{u}$  is the velocity of the fluid,  $\rho$  is the fluid density,  $p$  is the pressure,  $\mu$  is the dynamic viscosity,  $\vec{F}_{ST}$  is the surface tension and the subscript  $i$  corresponds to the appropriate phase. To track the movement of the interface between the two fluids, the level set method was used. In the level set method, the discontinuity between the two discrete phases is represented with the level set function  $\phi$ , a continuous function that represents the distance from the interface at all points in the domain. The continuity of this function allows the system to handle large deformations of the interface, including splitting into multiple functions. This function is commonly taken to be a smoothed Heaviside function, with 0 representing one fluid and 1 representing the other fluid. The  $\phi = .5$  isocontour then represents the interface between the two phases [25]. As the flow field is calculated, the interface is advected by:

$$\frac{\partial \phi}{\partial t} + \mathbf{u} \cdot \nabla \phi = \mathbf{0} \quad (3.3)$$

The discontinuity in density ( $\rho$ ) and viscosity ( $\nu$ ) are smoothed across the interface using Eqns. 3.4 & 3.5:

$$\rho = \rho_1 + (\rho_2 - \rho_1)\phi \quad (3.4)$$

$$\nu = \nu_1 + (\nu_2 - \nu_1)\phi \quad (3.5)$$

where  $\rho_1$  and  $\nu_1$  are the density and kinematic viscosity of the first fluid, and  $\rho_2$  and  $\nu_2$  are of the second fluid. The surface tension term, in Eqn 3.2, at a point  $\vec{x}$  can be calculated from:

$$\vec{F}_{ST}(\vec{x}) = \sigma \kappa(\vec{x}) \hat{n}(\vec{x}) \quad (3.6)$$

where  $\sigma$  is the surface tension coefficient,  $\hat{n}$  and  $\kappa$  are the unit normal and curvature of the interface, respectively. In the level set method,  $\hat{n}$  and  $\kappa$  can be calculated from

$\phi$  using:

$$\hat{n} = \frac{\nabla\phi}{|\nabla\phi|} \quad (3.7)$$

$$\vec{\kappa} = -\nabla \cdot \left( \frac{\nabla\phi}{|\nabla\phi|} \right) \quad (3.8)$$

The surface tension equation can then be recast in terms of the surface tension coefficient and the level set function:

$$\vec{F}_{ST}(\vec{x}) = \sigma \left( -\nabla \cdot \frac{\nabla\phi}{|\nabla\phi|} \right) \nabla\phi \quad (3.9)$$

In this formulation, the surface tension represents a volume force that is spread across the width of the interface. This new force is only equal to the surface tension in the limit as the thickness of the interface goes to zero, which places an upper bound on the maximum width of the interface. If the interface gets too small, however, the discontinuity in density and viscosity cannot be properly smoothed, which yields difficulties in computing the solution.

The general solution algorithm then, is to calculate the velocity of the flow using the momentum transport equation. Next, this velocity is used to advect the level set function, which modifies the shape of the interface. The curvature of the updated interface is then used to calculate the surface tension force. This updated surface tension force is then used at the next time step to solve the momentum equation.

One drawback of the level set method, in its standard formulation, is that it is not mass conservative. At each successive time step, as the interface is moved it is possible for it to move a greater distance than intended, which causes an inaccurate reporting of the volume. [26]. In Olsson *et al.* a modified version of the level set was developed to improve the mass conservation. In this method the movement of the level set function ( $\phi$ ) is corrected by using a modified advection equation:

$$\frac{\partial\phi}{\partial t} + \mathbf{u} \cdot \nabla\phi = \gamma \nabla \cdot \left( \epsilon \nabla\phi - \phi(\mathbf{1} - \phi) \frac{\nabla\phi}{|\nabla\phi|} \right) \quad (3.10)$$

where  $\gamma$  represents a re-initialization parameter that predicts where the interface has moved to since the last time step and  $\epsilon$  represents an estimated interface thickness. For numerical stability, the minimum mesh size should be  $O[\epsilon]$  and  $\gamma$  should be roughly equivalent to the maximum velocity of the flow. When  $\epsilon$  and  $\gamma$  are properly selected, nearly perfect mass conservation is expected [27],[28]. The CFD program, COMSOL Multiphysics was selected to perform the simulations. COMSOL is a finite element based solver, which uses the mass-conservative formulation of the level set method.

### 3.1.1 Boundary Conditions

The inlet boundary conditions for the computational model were selected to as closely resemble previous experimental work as possible. In the flow visualization experiments the gas and liquid phases are pressurized at 30 *psi*, and the slug lengths are controlled by decreasing the air inlet pressure from this baseline. In the computational model, however, inlet velocity conditions were instead used as they proved to be numerically stable over a wide range of inlet conditions. To find the necessary inlet velocity to compare to the pressure range used in McCabe *et al.* [20] a hydrodynamic analysis of the microfluidic channel was performed. This analysis is done assuming that the flow is entirely propellant with no inert gas. What follows is the classical Poiseuille flow given by:

$$\Delta P = Q * R_{Hyd} \tag{3.11}$$

where  $\Delta P$  is the upstream gage pressure,  $Q$  is the volumetric flow rate of propellant, and  $R_{Hyd}$  is the hydraulic resistance of the microchannel. This leaves two unknowns,  $Q$  and  $R_{Hyd}$ , that can be directly calculated using a few more relations. First, hydraulic resistance requires the knowledge of the microchannel geometry (length and

cross-sectional area) as well as the working fluids viscosity. The viscosity of HTP is 1.245 cP at 20° C. The microchannel geometry will be shown in greater detail in the following chapter, however for this analysis the length, L, is 90.28 mm and the area, A, is 50  $\mu m$  in width by 20  $\mu m$  in depth. Because of large surface-to-volume ratios in microchannels the simple hydraulic resistance calculation for non-circular cross-sections was reexamined by Mortensen *et al.* [29]. They rewrite the hydraulic resistance such that,

$$\alpha = \frac{R_{hyd}}{R_{hyd}^*} \quad (3.12)$$

where  $R_{hyd}^* = \mu L/A^2$  is a hydraulic resistance given by dimensional analysis and  $\alpha$  becomes a dimensionless geometrical correction factor. For this case,  $\alpha$  is a function of the compactness, C, which for a rectangular cross-section is given by Equation 3.13:

$$\alpha(C) \approx \frac{22}{7}C - \frac{65}{3} + O(|C - 18|^2) \quad (3.13)$$

Plugging all this in one finds a hydraulic resistance of 8.755  $\frac{psi}{\mu l/min}$  (units were chosen for simplicity in further calculations). These results compare well to tests run to experimentally determine the hydraulic resistance by McCabe [24]. The analytical value is comparable to the experimentally measured value of 8.25  $\frac{psi}{\mu l/min}$ . Using this hydraulic resistance, the estimated flow rate and thus the estimated inlet velocity can be calculated. For the range of pressures calculated studied by McCabe, the inlet velocity of the liquid phase is .38m/s. For the simulations inlet velocities of .4  $\frac{m}{s}$  for all inlets were roughly similar to the 30 *psi* baseline, and decreasing the gas inlet velocity by .05  $\frac{m}{s}$  resulted in a drop of pressure of roughly .1 *psi*.

In addition to the inlets and outlets, the appropriate boundary conditions for the walls must be determined. Typically, in CFD simulations, no-slip conditions are imposed at the walls to account for the effects of friction. In the level set method,

a no-slip condition would be inaccurate, because it would prevent the interface from moving along the walls. To account for this, there is a “wetted wall” boundary condition implemented within COMSOL. This boundary condition uses a slip length, which allows the interface to move along the wall, but adds a friction term to account for the walls:

$$\vec{F}_{fr} = -\frac{\mu}{\beta}\vec{u} \quad (3.14)$$

where  $\mu$  is the dynamic viscosity of the liquid,  $\vec{u}$  is the velocity of the fluids and  $\beta$  is the slip length, which is typically equal to the width of a single finite element. The contact angle is used to determine the shape of the interface at points where it comes in contact with the walls. In COMSOL, the contact angle is defined according to the diagram in Figure 3.1:

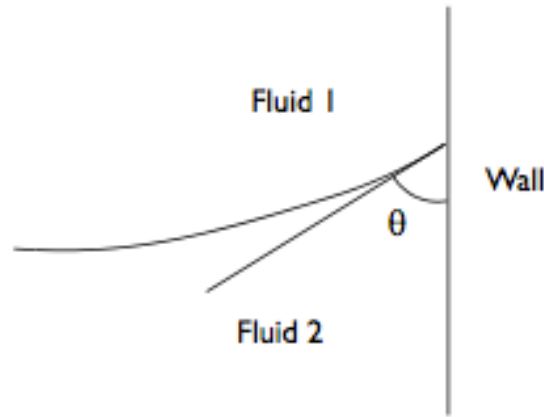


**Figure 3.1:** Definition of the contact angle,  $\theta$  within COMSOL.

## 3.2 Computational Implementation

COMSOL Multiphysics was used to perform the CFD analysis on the system. The following sections describe the selection of the baseline material properties, model geometry and computational grid used for these studies.

### 3.2.1 Baseline Material Properties

As the goal of this study is to examine the behavior of the slug-generation process over a range of parametric conditions, it was first necessary to establish a baseline simulation, against which further parametric studies could be compared. The liquid for these simulations was 90% hydrogen peroxide, while  $N_2$  was selected as the gas for the simulations. Table 3.1 below shows the default values for the parameters of interest.

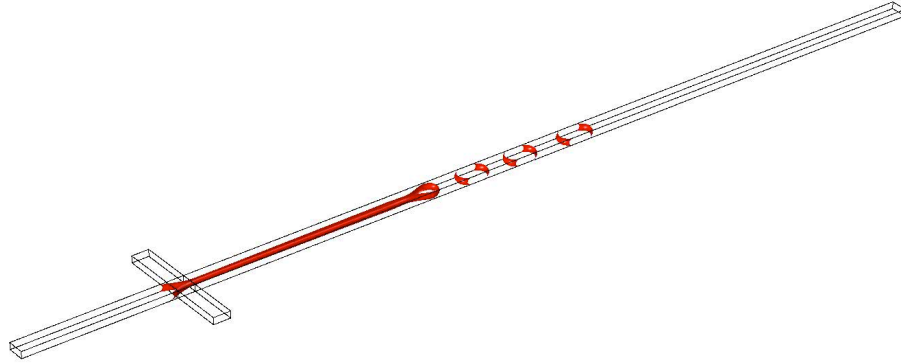
**Table 3.1:** Properties of  $H_2O_2$  and  $N_2$  at STP

Fluid	$H_2O_2$	$N_2$
Viscosity (cP)	1.245	.018
Surface Tension ( $\frac{dyn}{cm}$ )	79.0	–
Contact Angle (Degrees)	180	–

### 3.2.2 2D vs. 3D Results

Due to the intense computational demands of simulating the flow in 3D, using a 2D simulation was desirable for parametric studies. In Qian and Lawal [30], a strong connection between the 2D and 3D simulations of micro-slug generation in microchannels was found. To verify that a similar connection exists in this study, a 3D model of

the junction was simulated. An isosurface, and surface plot of these simulations are presented in Figure 3.2 below:



(a) Isosurface plot of the .5 contour of the level set function in 3D



(b) Surface plot of the level set function in 3D

**Figure 3.2:** Plots of the 3D simulation of the baseline case.

Next, these results were compared against the 2D baseline model. A surface plot of the 2D and 3D simulations of the baseline case are provided below:

The 2D models over-report the slug length compared to the 3D case by 11%; one cause of this error was assumed to be the lack of friction that would occur in the top and bottom of the channel. To account for this friction a body force term that accounts for the friction of the liquid of the top and bottom of the channel was added. This term, which is implemented in COMSOL as a correction for shallow channels, is:

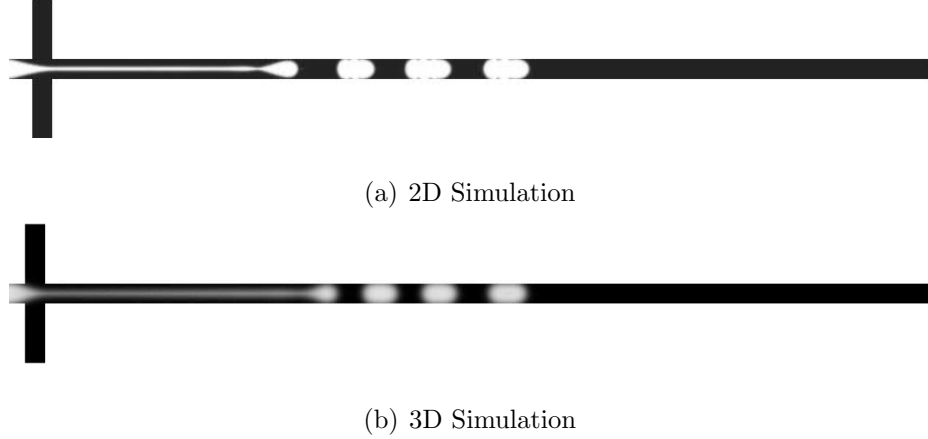


**Figure 3.3:** Comparison of the surface plots of the level set function for the 2D and 3D cases.

$$\vec{F}_{SC} = \frac{12\mu\vec{u}}{\rho h^2} \quad (3.15)$$

where  $\mu$  is the viscosity,  $\vec{u}$  is the flow velocity,  $\rho$  is the density and  $h$  is the height of the channel. Using this correction term resulted in slug lengths that are more in line with the 3D simulations.

### 3.2.3 Computational Domain & Grid Resolution Studies

The geometry of the computational model was selected to matchup with the microchannel used in McCabe *et al.* [20] for comparison purposes. This microchannel, shown in Figure 3.4, is  $50 \mu m \times 20 \mu m$ , with the distance from the liquid inlet ports to the junction of  $3 mm$  and the distance from the gas inlet port to the junction of  $6 mm$ . To reduce the computational domain, the inlet lengths were truncated to  $150 \mu m$  and  $300 \mu m$  respectively. The resulting domain is shown in Figure 3.4b. To account for the affects along the length of the channel that is not simulated, a laminar inflow boundary condition is implemented. In COMSOL, this boundary condition calculates the pressure drop and velocity profile of the channel and uses that as the

inlet values for the simulation. The outlet channel, which contains the microslugs, is truncated from 80 *mm* on the microchannel to 2200  $\mu\text{m}$  in the simulation, with a laminar outflow boundary condition used to account for the downstream effects that are outside of the computational domain.

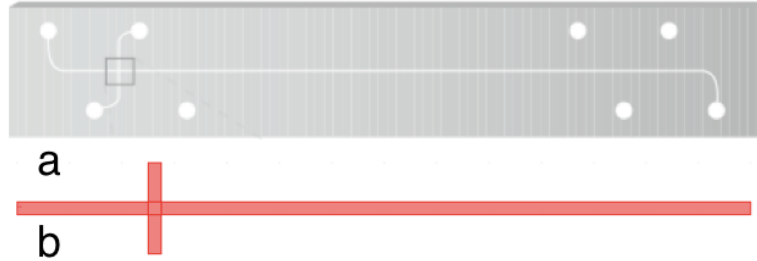


**Figure 3.4:** (a) The geometry of the microchannel used for flow visualization experiments. (b) The geometry of the computational domain that corresponds to the junction outlined in (a).

To demonstrate that the results generated were independent of the downstream portion of the system, that are not being directly simulated, a model with an increased downstream domain (4500  $\mu\text{m}$ ) was also simulated. A comparison of the length of the first slug in both the “short” and “long” downstream domain are presented in Table 3.2, where the uncertainty is because the computational grid cannot be fully resolved on a per pixel basis:

**Table 3.2:** Comparison of the initial slug in the “short” and “long” computational domains

	Slug Length ( $\mu\text{m}$ )	Standard Deviation
Short	139	4.63
Long	142	4.24
Percent Difference	2%	9%

The similarity between the two simulations illustrates that the laminar outflow

boundary condition is sufficient to account for the portion of the domain that is not being explicitly simulated, with dramatically reduced overhead.

While using the short channel provides a drastic reduction in processing time required, it does impose some limitations on the simulation. Specifically, the laminar outflow boundary condition is unable to simulate the interface as it exits the domain. For this reason, all simulations are limited in duration to the point where the first gas bubble reaches the outlet of the domain. This occurs between .018 - .025 *s* depending on the inlet boundary conditions. This is typically long enough to generate 10-20 slugs. In Section 3.4.2 analysis was performed to demonstrate that this is enough slugs to use for statistical analysis.

As discussed in section 3.1, a primary concern when using the level set method is interface width, which directly impacts the grid selection. If the grid is too large the interface, and thus the density and viscosity, are too diffuse and provide non-real results. Decreasing the grid size eliminates this problem but can lead to a dramatic increase in the number of finite elements, which leads to an increase in computation time. In Olsson *et al.* [27], a methodology for finding grid independence for the conservative formulation of the level set was proposed. The primary consideration in this method is the mass conservation during successive iterations. To find this, the volume of a single bubble is plotted as a function of time; at a sufficiently fine grid this plot should be linear. The baseline simulation case was run for three different grids with the results plotted in Figure 3.5 below:

For the computational domain, 13,950 elements results in a real-time simulation of roughly 18 hours for a simulation of .018 *s*. Based on the convergence of results between the 6200 and 13,950 element grid, as well as the conservation of mass for 13,950 elements, this was selected as the grid for the simulations.

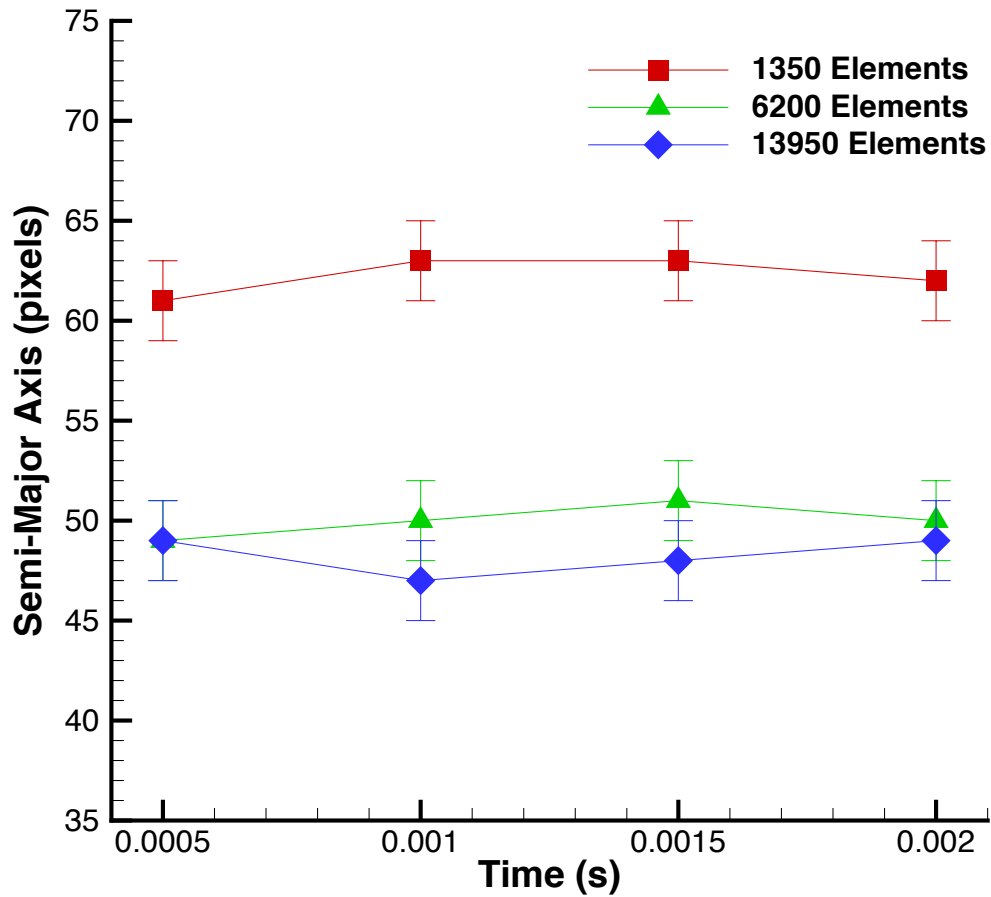


**Figure 3.5:** Plot of the slug length as a function of time for various grids.

### 3.3 Experimental Setup

To provide a baseline comparison for numerical simulations, a limited set of experimental data was collected using the procedure developed by McCabe. [20] These comparisons were used to confirm that the general results being created in the simulations were in line with the experimental data.

In McCabe [20], a pressure-driven microfluidic flow system was developed to study the microslug formation process. This system uses water for the liquid phase and air

for the gas phase; these are selected for their accessibility and chemical similarity to  $H_2O_2$  and  $N_2$  respectively as shown in Table 3.3:

**Table 3.3:** Comparison of relevant material properties used in the simulations and experiments

Fluid	$H_2O_2$	$H_2O$	$N_2$	<i>Air</i>
Viscosity (cP)	1.245	1.0016	.0178	.0183
Surface Tension ( $\frac{dyn}{cm}$ )	79.0	72.7	–	–

The microfluidic chip that contains the flow channels is manufactured offsite by Micralyne Inc. The chip is made of Schott Borofloat glass allowing for optical analysis. The top surface of the chip has four access holes three of which lead to channels that merge into a  $90^\circ$  junction and a fourth serves as the outlet. The channel width and depth are  $50 \mu m$  and  $20 \mu m$ , respectively. Figure 3.6 shows the channel cross section and a 2-D model of the microchannel chip. The microchannels are etched using a chemical etch technique generating the geometry shown in the figure. Chemical etching of Borofloat glass is an isotropic etch meaning that the etchant penetrates the substrate at the same rate in all directions. The tubing used to connect to the Micralyne chip is a PEEK<sup>TM</sup> polymer tubing of 1/16 outer diameter and 0.015 inner diameter. PEEK<sup>TM</sup> provides the rigidity needed as well as being produced in the 1/16 outer diameter size required for the ports. Upchurch Scientific NanoPorts<sup>TM</sup> provide a 10-32 threaded connection between the PEEK<sup>TM</sup> tubing and the access (via) holes on the Micralyne chip. These ports have a high pressure adhesive ring to bond the port to the substrate and a small O-ring is seated around the access hole creating the hermetic seal. A schematic of the full system can be seen in Figure 3.7.

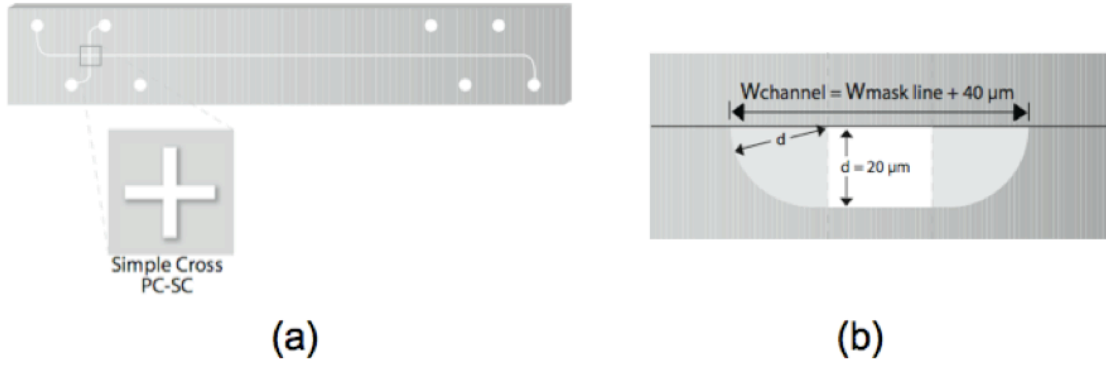


**Figure 3.6:** a) Schematic of the microchannel chip layout. The insert shows the four-way junction. b) Schematic of the microchannel cross section. The width of the mask line is  $10 \mu\text{m}$ . The top piece of glass has the access holes and the bottom piece has the etched pattern. The two are fused together in the final steps of the manufacturing process.

### 3.4 Data Analysis

The goal of this study is to characterize the thruster characteristics, thrust and impulse bit, as a function of varying parameters. To that end, it is necessary to isolate the flow characteristics that are expected to vary during a simulation. To find the thrust generated, assuming 100% efficiency in  $H_2O_2$  decomposition, no viscous losses in the micronozzle and no transient effects, was calculated using:

$$F_t = (\rho L_s A_c f) I_{sp} g_0 \quad (3.16)$$

where  $L_s$  is the average slug length,  $A_c$  is the cross-sectional area of the channel,  $f$  is the slug formation frequency,  $I_{sp}$  is the specific impulse of the monopropellant and  $g_0$  is the acceleration due to gravity. The  $I_{sp}$  of  $H_2O_2$  is listed as  $154s$ . In Equation 3.16,  $L_s$  and  $f$  are the only values that we expect to vary. For completeness, the thrust contribution of the inert gas was also considered. Cold gas thrusters typically have  $I_{sp}$  values on the order of  $70s$  or roughly half that of the  $H_2O_2$ . However, the mass flow rate of the gas in this system is several magnitudes smaller than the liquid

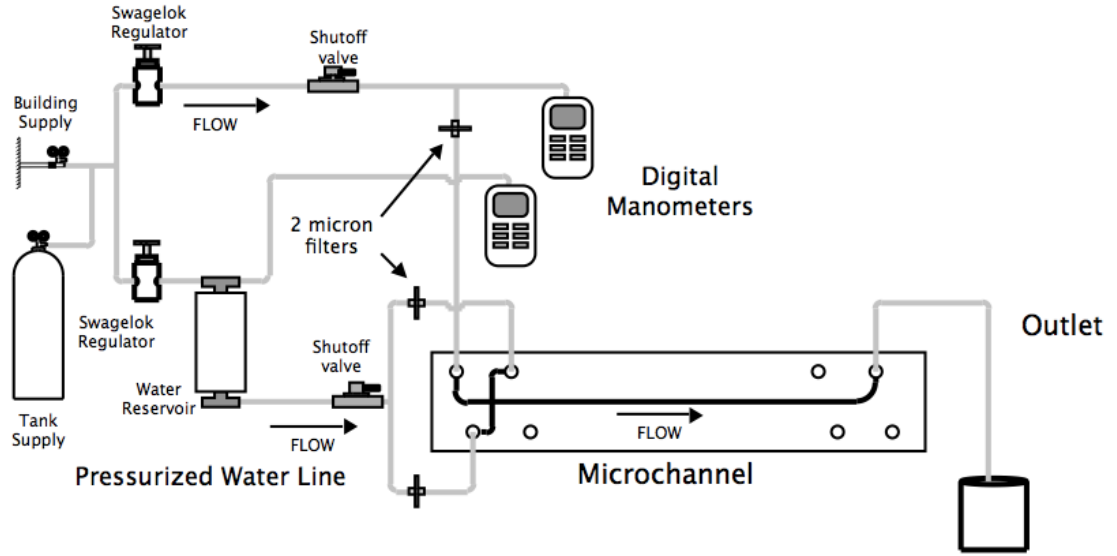


**Figure 3.7:** Layout schematic for the pressure supply system with locations of filters and measurement devices.

phase. Therefore the gas contribution to the thrust can be neglected.

In a similar manner, the impulse per slug was calculated by dividing the total thrust by the frequency, which makes it dependent only on slug length.

$$I_{per\ slug} = (\rho L_s A_c) I_{sp} g_0 \quad (3.17)$$

The impulse bit can be calculated by multiplying the microvalve response time by the formation frequency, to determine the number of slugs, which can then be multiplied by the impulse per slug to find the total impulse bit achievable. As this metric is necessarily dependent on the microvalve response time, for the duration of this paper the key metric will be impulse per slug.

From Equations 3.16 and 3.17, it is clear that the two quantities necessary to find the thrust and impulse bit are slug length and formation frequency. The following sections describe the steps taken to calculate these two quantities.

### 3.4.1 Data Collection

Using the methods described above, a 2D surface plot of the level set function is plotted in black and white, where anything less than .5 represents liquid, anything greater than .5 represents gas and the .5 isocontour, by definition, represents the interface between the two. An example surface plot is provided in Figure 3.8.



**Figure 3.8:** Sample surface plot of the baseline simulation. The liquid is represented in black, and the gas is represented in white.

For consistency, all plots are performed at .018 s, which represents the point immediately before the first slug leaves the domain at the maximum velocity case. These plots are output as JPEG files for analysis in MATLAB.

A MATLAB script, listed in Appendix B, was created to import and analyze the COMSOL surface plots. A block diagram of the MATLAB code is laid out in Figure 3.9.

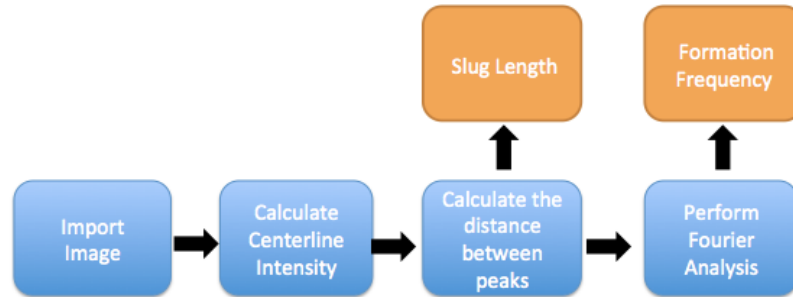


**Figure 3.9:** Block diagram showing the general process of the MATLAB script. The outcomes are highlighted in orange.

The JPEG images are imported and the image is truncated to the center of the

channel. To prepare for frequency analysis the DC component of the signal is removed by taking an average of the entire image matrix and subtracting it from each matrix value. Then all signals are averaged together to minimize any possible influence of random intensity variations. Next, the intensity is plotted, which results in a square wave. To measure the length of the slugs, the distance between leading edges of the square waves are calculated. The average of each of these distances is then saved as the average slug length. Next, the pinch-off frequency is computed using a discrete-time Fourier transform routine within MATLAB. The intensity signal is collected from the image reconstruction as discussed in the previous section. Again, to reduce the variance of the spectrum the DC component of the intensity signals is removed and then each of the signals are averaged together. The power spectral density of the signal is calculated using the FFT algorithm, then normalized and plotted. This is done first using spatial frequencies related by the pixel number. Once the densities are calculated based on spatial frequencies a simple substitution is used to convert over to temporal frequencies. The relation between time and space (pixel space) is given by:

$$t = \frac{\text{pixel number}}{\text{frame rate}} \quad (3.18)$$

where frame rate is in units of frames per second.

### 3.4.2 Slug Length Analysis

Typical simulations include 10-20 discrete slugs that form during the course of the simulation. The methods developed for analyzing these slugs involve averaging the length of the slugs and performing Fourier analysis to find the formation frequency. This was done by comparing the standard deviation in slug length divided by the average slug length to find the coefficient of variation, where the uncertainty in the

length of the microslugs comes from the lack of resolution in the images:

$$\text{Coefficient of Variation} = \frac{\text{Standard Deviation}}{\text{Average Slug Length}} \quad (3.19)$$

In these studies, two types of periodic flows occurred: regular, periodic flow characterized by slugs that had a coefficient of variation less than 5% and a flow regime where consecutively numbered slugs would be periodic such that “odd” numbered slugs are similar, and “even” numbered are similar, both with a coefficient of variation less than 5%. In typical thruster operation, hundreds of slugs may be produced for a single maneuver, so these variations will become irrelevant.

Based on the similarity of slugs in both configurations, using average slug length for the statistical calculations was deemed appropriate. All lengths reported in this paper are averages of the finite number of slugs produced in the simulations.

### 3.4.3 Slug Volume Analysis

In Chapter 2, the mass flow rate of the microslugs was presented as:

$$\dot{m} = (f * L_s * A_c * \rho)$$

where  $f$  is the formation frequency,  $L_s$  is the length of a microslug,  $A_c$  is the cross-sectional area of the microchannel and  $\rho$  is the density of the fuel. This formulation, first presented in McCabe [24], allows for the calculation of a mass flow rate using only an average slug length. This formulation was ideal for the experimental procedures, as it required a single measurement per slug, which could be taken along the centerline of the channel, where the image was least distorted. There are some errors involved in this calculation, as this method underestimates the volume of a microslug by estimating it as a perfectly rectangular quadrhedron. McCabe [24] reported the

error associated with this estimate as between 1% and 6%, depending on the length of the slugs.

In this study, the goal was to use techniques that would work experimentally to analyze simulations. This would allow for more direct comparison of results, as well as prevent errors introduced from using different analytical techniques. One drawback with using this technique, however, is that it limits the accuracy of the simulations; while it is difficult or impossible to calculate the area of an experimental microslug due to optical distortion and uncertainty around the interface, in simulations this is a trivial calculation. The goal of this section is to calculate the volume of a single, simulated microslug in two different ways. These results will then be compared to the reported volume of the slug found from the simulation software.

To make these comparisons, the baseline parameters were simulated in 3D. The results of these simulations were plotted as 2D contour plots, shown in Figure 3.8, and these images were analyzed.

The first method calculated was the linear method, which was used throughout the remainder of this study. This

The second method used to calculate the volume of the slug was an area analysis of the 2D image. In this method, the area integral was approximated as a Riemann sum of the black pixels, representing the fuel:

$$\int \int \phi \, dx \, dy = \sum_{i=1}^n \sum_{j=1}^m \phi \, \Delta x \, \Delta y \quad (3.20)$$

In practice, this was done in MATLAB by counting the number of black pixels in the region of interest. These pixels were then multiplied by the area per pixel to generate a total area for the slug. Next, this slug area was multiplied by the height of the microchannel to generate a total volume.

For comparison, the volume of the microslug was calculated in COMSOL using a

built in volume integration. Similar to the area integration presented above, this volume integration is done by summing each of the finite elements representing the fuel (i.e.  $\phi > .5$ ). While this is the most result, it is important to note that due to experimental constraints, this method would be impossible to duplicate with experimental data.

The results of these three methods are presented in Table 3.4 below, along with a comparison of the difference of the 1D and 2D calculations to the 3D method. As expected, the 1D and 2D results underestimate the volume of the microslug, with the 1D 8.3% below and the 2D 2.1% below.

**Table 3.4:** Comparison of the different slug volume calculation methods

Method	Volume ( $m^3 \times 10^{-13}$ )	% Error from 3D
Linear	2.0426	8.3
Area	2.1808	2.1
Volume	2.227	–

While these results demonstrate that there is a clear difference between the actual volume of the slug and the volume calculated using the linear method, it is worth noting that these results represent a worst case scenario. The baseline simulation, presented here, involve the shortest slugs that are seen in these simulations. As the slugs get longer, the ratio of the fraction of the slug that is being excluded by the linear method to the fraction of the slug that is being included by the linear method decreases.

The 2D approximation is much closer to the actual results, but requires the ability to fully resolve the microchannel in order to calculate it accurately. While this was not possible with the optical system used in McCabe [24], as the capabilities of the optical system improves, this technique would be a better method for calculating the

volume of experimental slugs.

### **3.4.4 List of Studies**

Using these methods parametric studies were performed, with surface tension coefficient, contact angle and viscosity as the parameters of interest. For each of the parameters two separate studies were conducted; the first held the inlet velocity for both phases constant at  $.4 \text{ m/s}$  while varying the parameter of interest. The second held the parameter of interest constant while lowering the gas inlet in steps of  $.05 \text{ m/s}$ . The full list of cases can be seen in the tables below.

**Table 3.5:** Surface Tension Coefficient Studies

---

Surface Tension (dyn/cm)	Velocity (m/s)				
	.20	.25	.30	.35	.4
50	x	x	x	x	x
60	x				
70	x	x	x	x	x
80	x				
90	x				
100	x	x	x	x	x

---

**Table 3.6:** Contact Angle Studies

---

Contact Angle (Degrees)	Velocity (m/s)				
	.20	.25	.30	.35	.4
150	x	x	x	x	x
155	x				
160	x				
165	x	x	x	x	x
170	x				
175	x				
180	x	x	x	x	x

---

**Table 3.7:** Fuel Viscosity Studies

Fuel Viscosity (cP)	Velocity (m/s)				
	.20	.25	.30	.35	.4
0.6	x				
0.8	x				
1.0	x				
1.2	x	x	x	x	x
1.4	x				
1.6	x	x	x	x	x
1.8	x				

# Chapter 4

## Results

A first step in checking the model, was to perform a qualitative comparison of the simulation data with data collected experimentally. The results of these comparisons are presented in Section 4.1, below.

To study the effects of surface tension, contact angle and viscosity on the slug length and formation frequency, parametric studies for each of these properties were conducted. The results of these studies, which are presented below, are then used to calculate the thrust and impulse per slug, which are also presented below.

### 4.1 Qualitative Comparison with Experimental Data

While direct quantitative comparison between the simulations and the experiments are not possible, due to the mismatch between the inlet conditions, there are clear qualitative similarities between the experimental and numerical result, shown in Figure 4.1. Specifically, the large channel filling bubbles, which are produced at a pinch-off location that is downstream from the junction and the region upstream of the junction, where the liquid and gas meet.

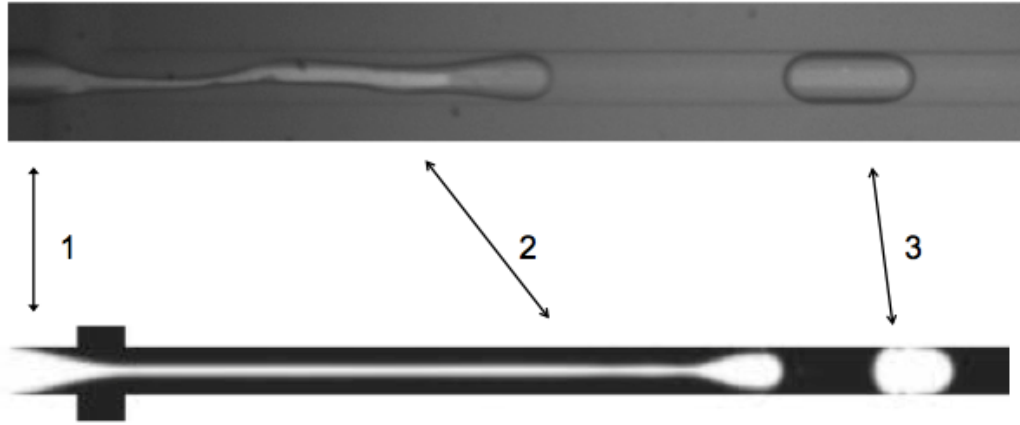


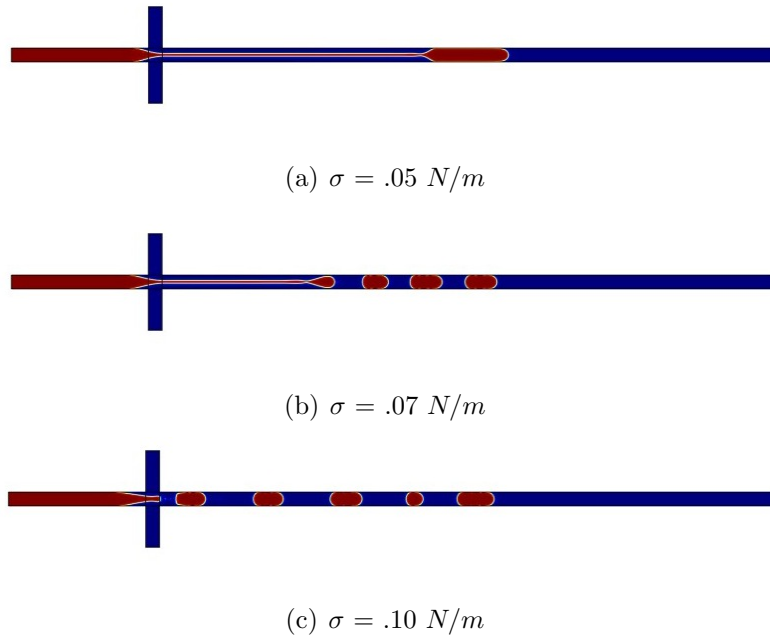
**Figure 4.1:** A qualitative comparison of the experimental and numerical results. 1) The upstream attachment mechanism. 2) The downstream detachment mechanism. 3) The large, channel filling bubbles.

The behavior of the slug formation was next studied experimentally and computationally as the gas pressure was lowered. In both cases, the decrease in the gas flow rate resulted in an increase in the slug length and a decrease in the slug formation frequency. Further decreases in the gas inlet velocity result in the channel completely filling with liquid, while increasing the gas velocity results in annular flow, where a center core of gas flows down the channel and is surrounded by liquid. This correspondence between the behavior of the simulations and experiments lends confidence to the results that the model is generating.

## 4.2 Impact of Surface Tension Variation

To determine the effects of surface tension on microslug formation, the surface tension coefficient was varied on a baseline simulation with  $\Delta V = 0$ , in steps of .01 N/m, from .10 N/m, corresponding to a high value for  $H_2O_2$  down to .05 N/m, beyond which the simulation show a transition to an annular flow regime, that does not produce slugs. This variation led to a range of slug sizes as shown in Figure 4.2. This flow simulation

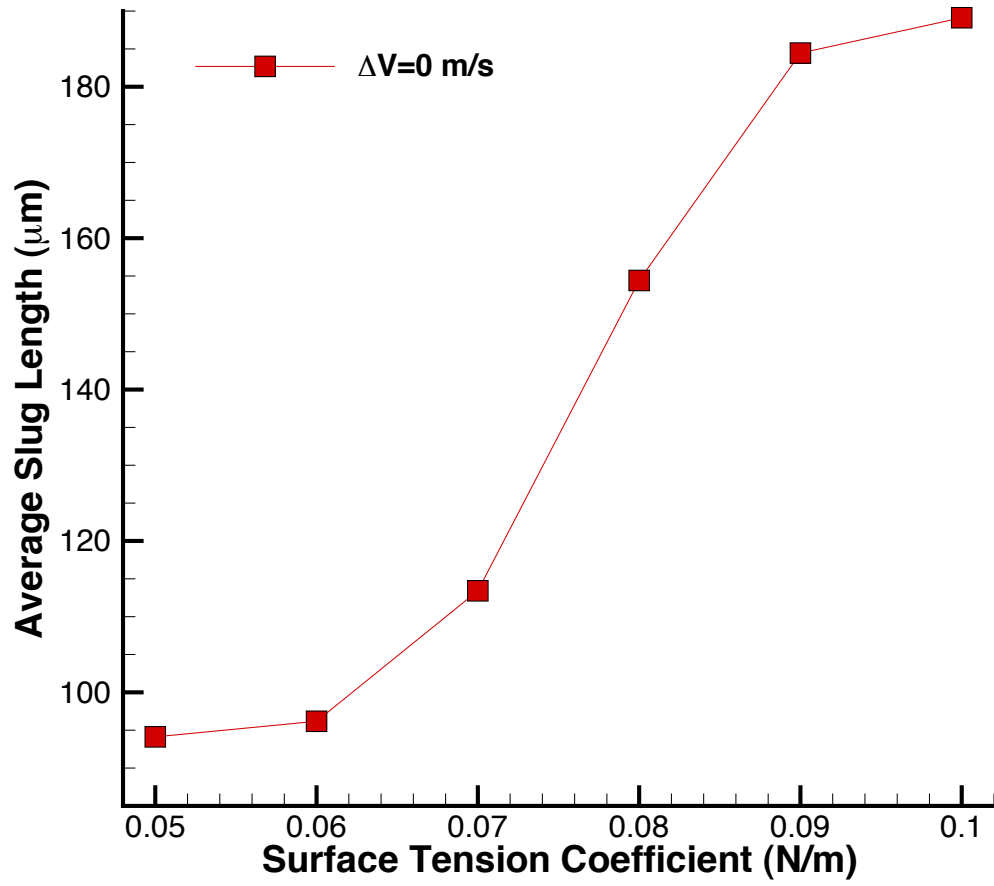
data was then analyzed to determine both slug size and formation frequency.



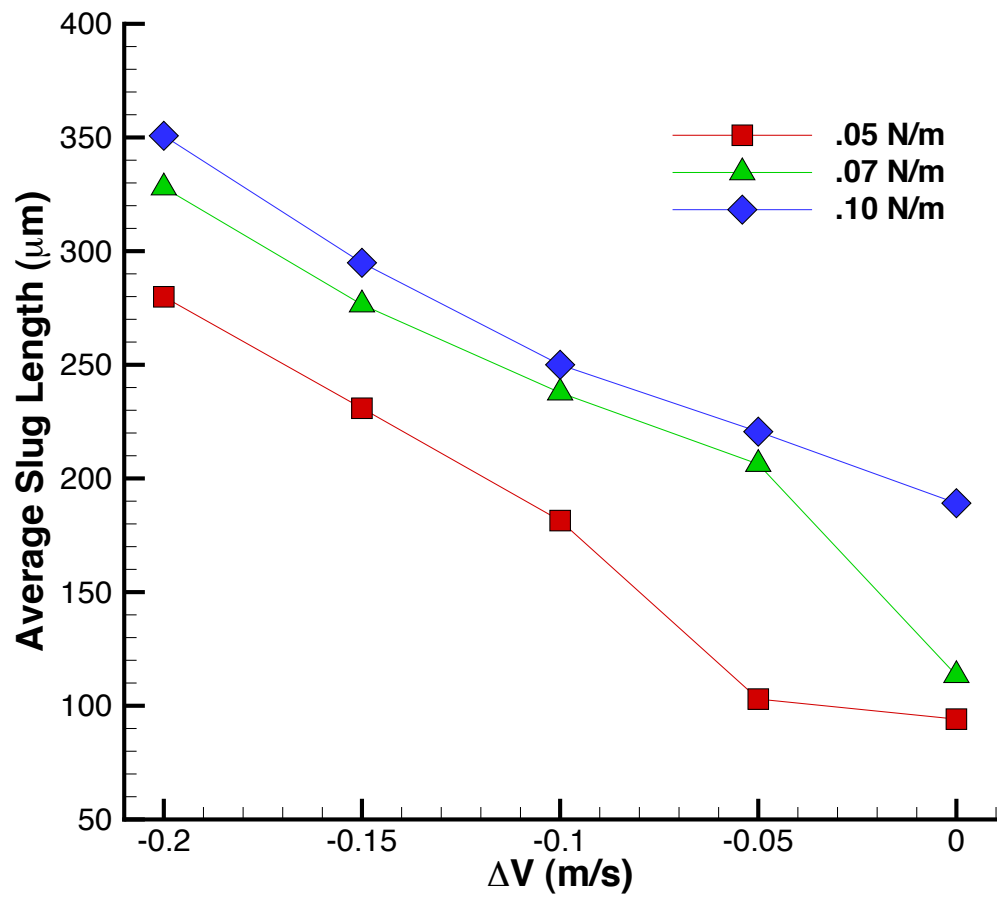
**Figure 4.2:** Sample of results generated by varying the surface tension coefficient with  $\Delta V = 0$  over an equivalent time period, with the simulated monopropellant in blue.

Figure 4.3 show the results of this analysis. At  $.05 \text{ N/m}$ , the first slugs are formed, and the slugs at  $.06 \text{ N/m}$  are very similar in size. Between  $.06 \text{ N/m}$  and  $.09 \text{ N/m}$ , the slug length increases rapidly with small changes in the surface tension coefficient. From  $.09$  to  $.10$  there is only a small change in the slug length. As the surface tension coefficient for  $H_2O_2$  typically ranges from  $.07$  to  $.09 \text{ N/m}$ , the region of increase dependence of slug length is important.

Figure 4.5 shows that the formation frequency is essentially bimodal, with surface tension coefficients below  $.07 \text{ N/m}$  having extremely low frequencies ( $>50 \text{ Hz}$ ), while there is a large jump to  $350 \text{ Hz}$  at  $.07 \text{ N/m}$  then appears to asymptote to a frequency around  $200 \text{ Hz}$ . The behavior of the formation frequencies between  $.07$  and  $.10 \text{ N/m}$  can be explained by looking at the mass flow rate of the slugs, which are proportional to the product of the formation frequency and the slug length. Between  $.07$  and  $.10$



**Figure 4.3:** A plot of slug length vs. surface tension coefficient for fixed  $\Delta V = 0$  and  $V_{liquid} = .4 \frac{m}{s}$



**Figure 4.4:** A plot of slug length vs.  $\Delta V$  for three different surface tension coefficients. This plot highlights the similarity of the results.

N/m this mass flow rate increases by only 11%.

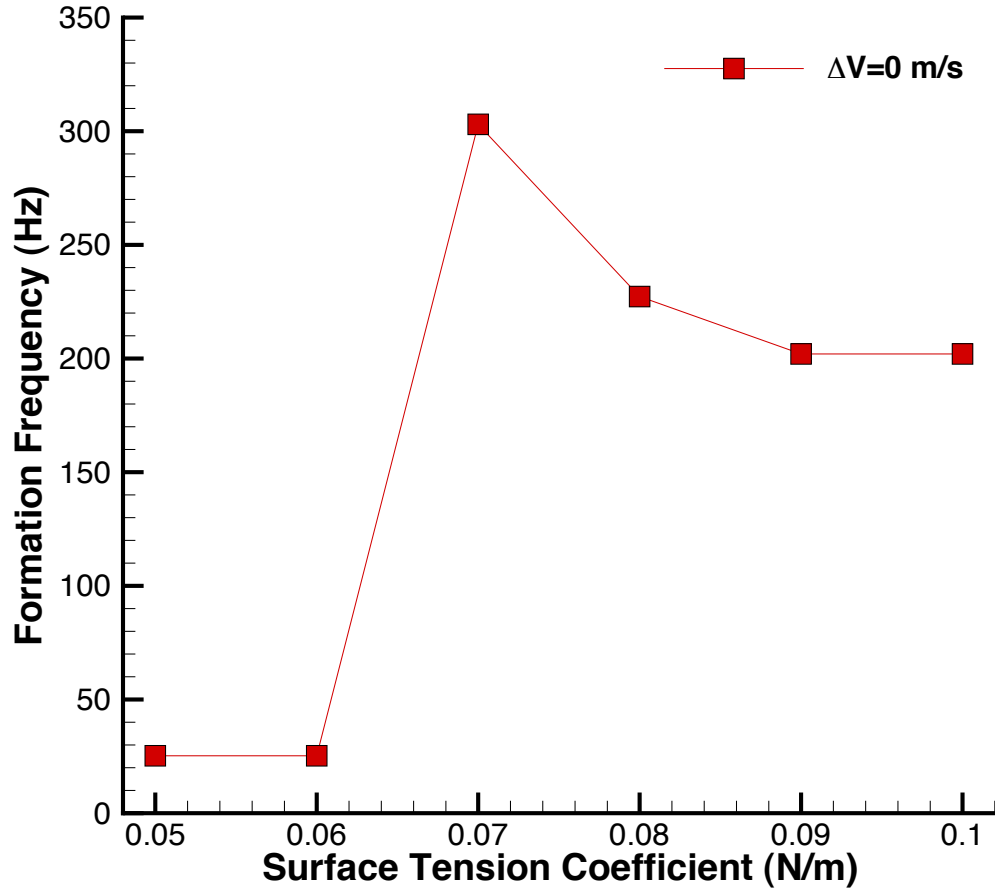


**Figure 4.5:** A plot of slug formation frequency vs. surface tension coefficient, for  $\Delta V = 0 \frac{m}{s}$ . There is a clear transition between  $.06 \frac{N}{m}$  and  $.07 \frac{N}{m}$ .

These two different modes occur because decreasing the surface tension coefficient has the effect of inducing the transition to annular flow for inlet parameters that would not typically result in annular flow. To better illustrate this point, the slug characteristics across a variety of inlet parameters were plotted for three surface tension coefficients (.05, .07 and .10 N/m) shown in Figure 4.4. These plots indicate

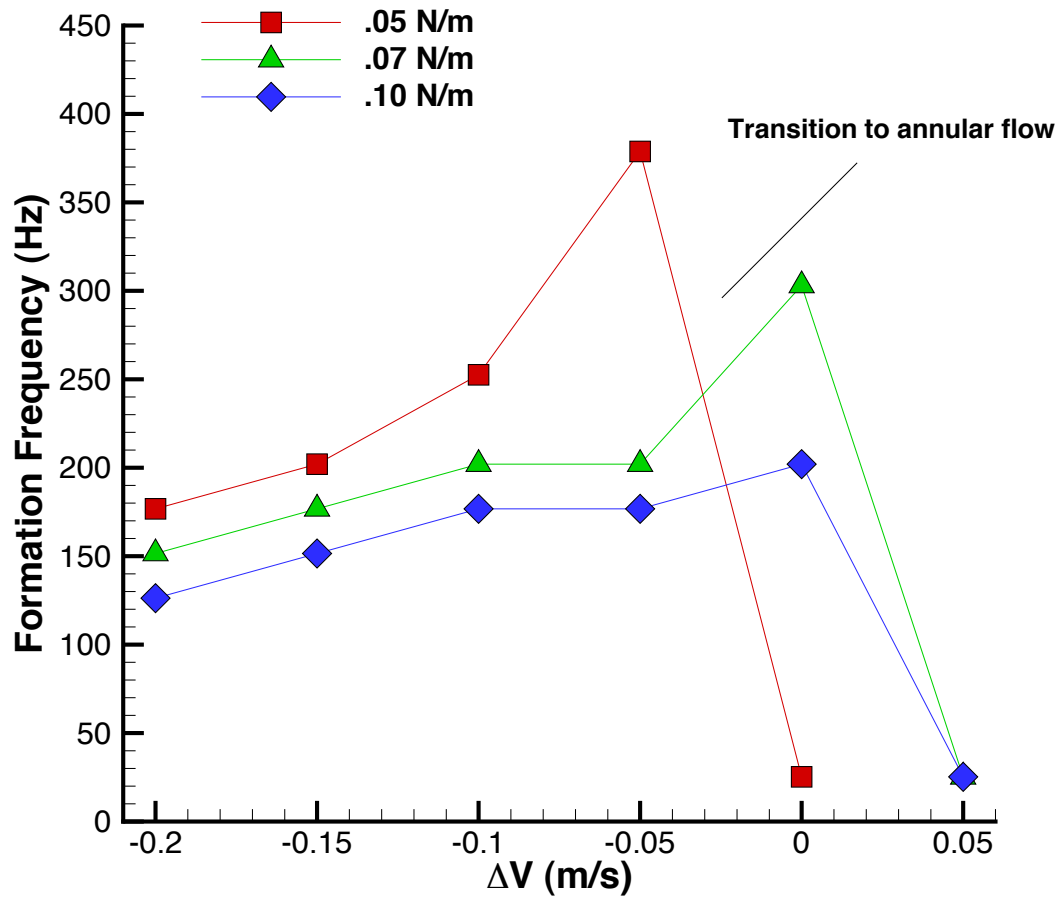


**Figure 4.6:** A plot of slug formation frequency vs  $\Delta V$  for three different surface tension coefficients. This plot highlights the similarity of the results.

that the effect of surface tension acts as an offset for the slug formation, where an increase in the surface tension coefficient has an effect similar to increasing the gas inlet velocity. Figure 4.6 shows the low surface tension coefficient case transitioning from slugs to annular flow for a lower gas inlet velocity.

### 4.3 Impact of Contact Angle Variation

The next parameter of interest was the sensitivity of slug formation to changes in the contact angle. Contact angle, which is a measure of the hydrophobicity of the surface of the microchannel, can be modified by contaminants in the liquid or imperfections in walls and could have an impact on the performance of the system. Shown in Figure 4.7 are plots of the slug size and formation frequency as a function of contact angle for a fixed inlet condition ( $\Delta V = 0$ ) and surface tension coefficient (.07 N/m). This plot indicates a bimodal structure with a transition between 150 and 160 degrees. The physical mechanism for this transition is readily observed in Figure 4.8, where the pinch-off location shifts from the junction ( $\leq 155$  Degrees) to a pinch-off located several channel widths downstream ( $>155$  degrees).

This shift in pinch-off location appears to be connected with the attachment point that exists upstream of the junction; as the contact angle varies the angle that this attachment point makes with the wall varies accordingly. For values of the contact angle equal to or below 155 degrees, the angle of this attachment results in slugs generated at the junction. As the contact angle increases, a critical value is reached at which the attachment point no longer results in slugs being formed at the junction, shifting to a downstream pinch-off. While dramatic shifts in the contact angle are unexpected during typical operation, this connection between the detachment point, and the corresponding slug length, indicates that the microchannel should be designed

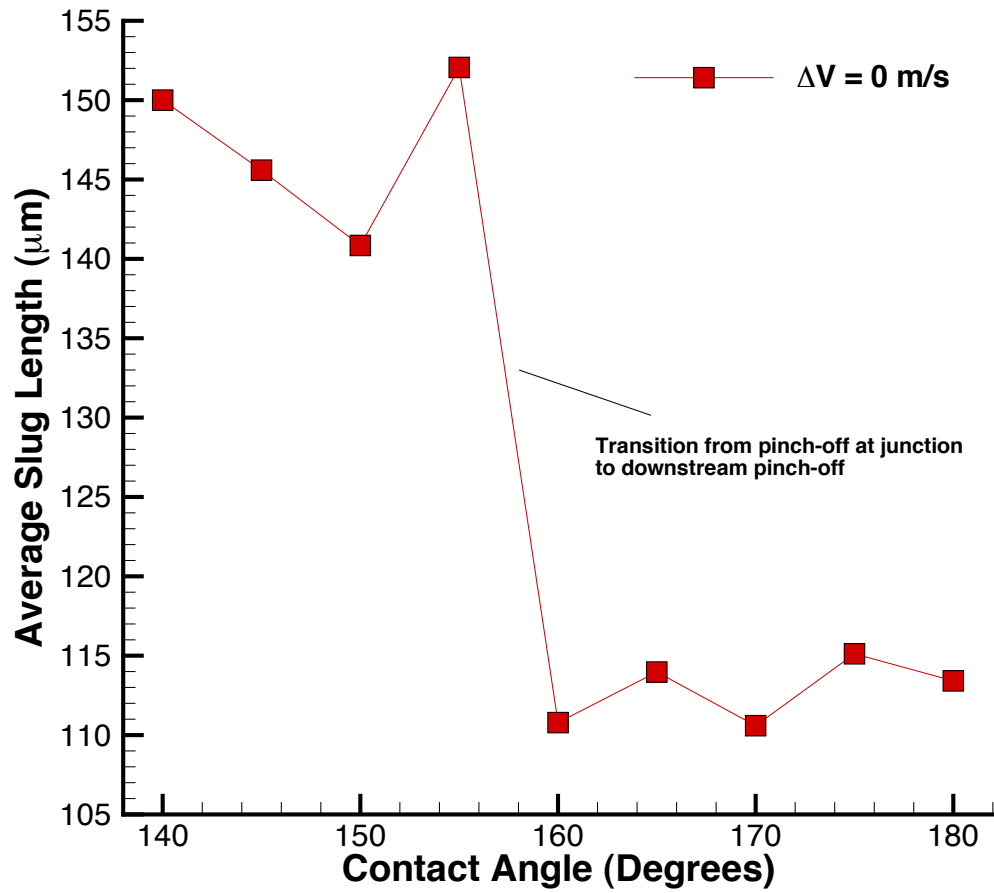
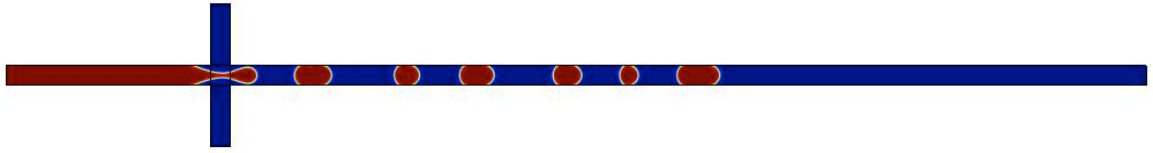
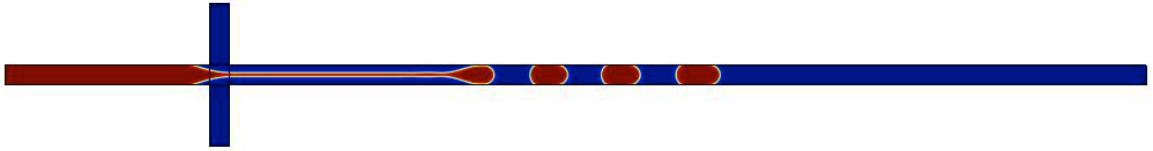


**Figure 4.7:** The plot of slug length as a function of contact angle. There is a clear transition between 155 and 160 degrees, which corresponds to a change in pinch-off mechanism.

to avoid this transition region.



(a) Contact Angle =  $155^\circ$



(b) Contact Angle =  $160^\circ$

**Figure 4.8:** Contour plots showing the change in detachment location that leads to change in microslug length.

Next, the system was simulated for three different contact angles as the air inlet velocity was increased. Figure 4.9 is a plot of the average slug length for 150, 165 and 180 degrees. This plot shows that increasing contact angle has an inconsistent effect on the slug length.

## 4.4 Impact of Thermally-Induced Viscosity Variation

The final parameter studied was the sensitivity of the system to minor changes in viscosity. In Cubaud *et al.*[31], variations in the viscosity ratio of the two fluids were shown to have a significant effect on the flow regime. Specifically, as the viscosity ratio of the liquid phase to the gas phase increases, there can be a transition from a slug forming regime to annular flow. As the viscosity of  $H_2O_2$  ranges from .6 cP at  $50^\circ$  C to 1.8 cP at  $0^\circ$  C, the microthruster may undergo significant changes in

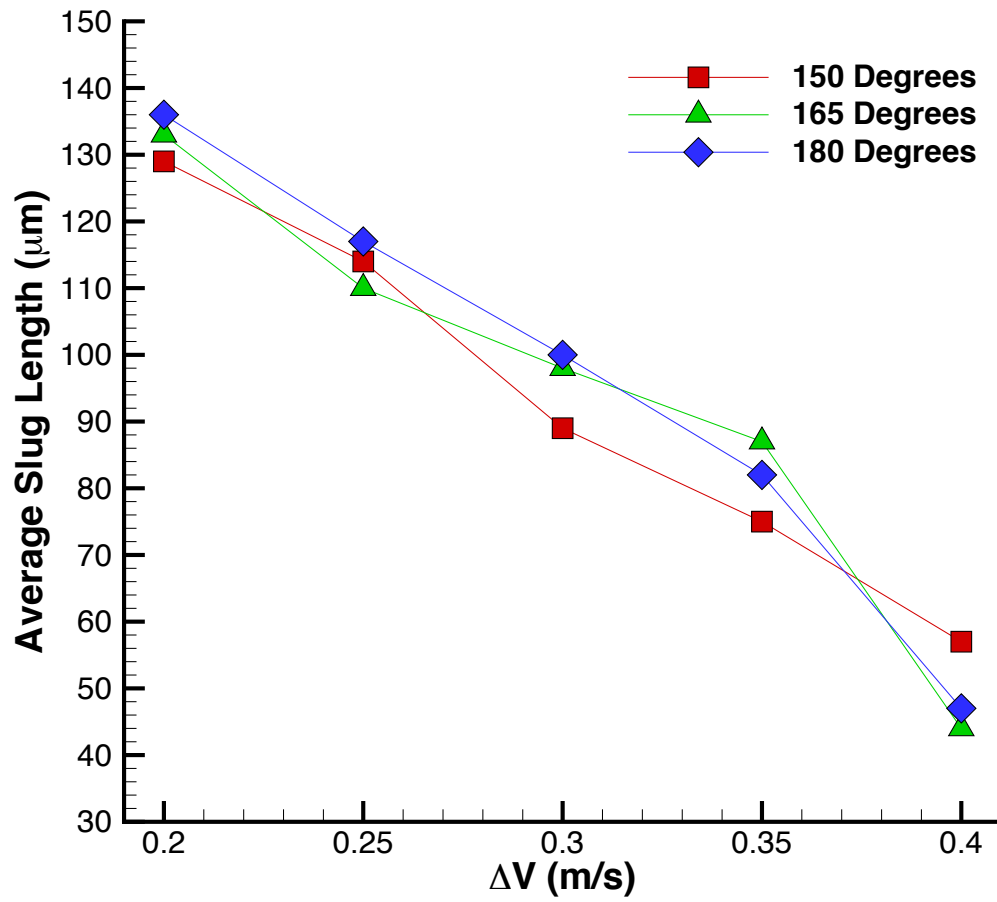


**Figure 4.9:** A plot of slug length vs.  $\Delta V$  for three different contact angles. This plot highlights the similarity of the results for these contact angles.

the viscosity ratio during operation. To determine the effects of these changes, the viscosity of the liquid phase was varied from .6 cP to 1.8 cP in steps of .2 cP.

Plots of the slug length and formation frequency for various viscosities are shown in Figures 4.10 and 4.11. From .6 to 1.6 cP there is a 47.16% reduction in slug length, but there is a smooth, nearly linear progression. At 1.8 cP, however, the system transitions from slug formation to annular flow in a manner that appears consistent with the work presented in Cubaud *et al.* As no slugs are formed, the slug length and formation frequency drop to zero in this case.

To understand the plot of formation frequency, it is again illustrative to look at the mass flow rate by taking the product of the slug length and formation frequency. When this is done, there are two distinct regions where the mass flow rate is relatively unchanged. In the first region, between .6 and 1.0 cP, the mass flow rate decreases by 6%. Between 1.0 cP and 1.2 cP, the mass flow rate decreases by 39%. Then, between 1.2 and 1.6 cP, the mass flow rate decreases by 19%.

Further studies were done to determine the relationship between slug formation and air inlet velocity as the viscosity of the fuel is increased. As shown in Figure 4.12, there is a strong similarity between the length of the slugs at 1.2 cP and 1.6 cP, with the increased viscosity acting to decrease the length of the slugs.

In Figure 4.13, the slug formation frequency is plotted for increasing air inlet velocity. The higher viscosity results in an increase in the slug formation frequency. The plot shows a clear similarity between the formation frequency of the system at the two different viscosities.

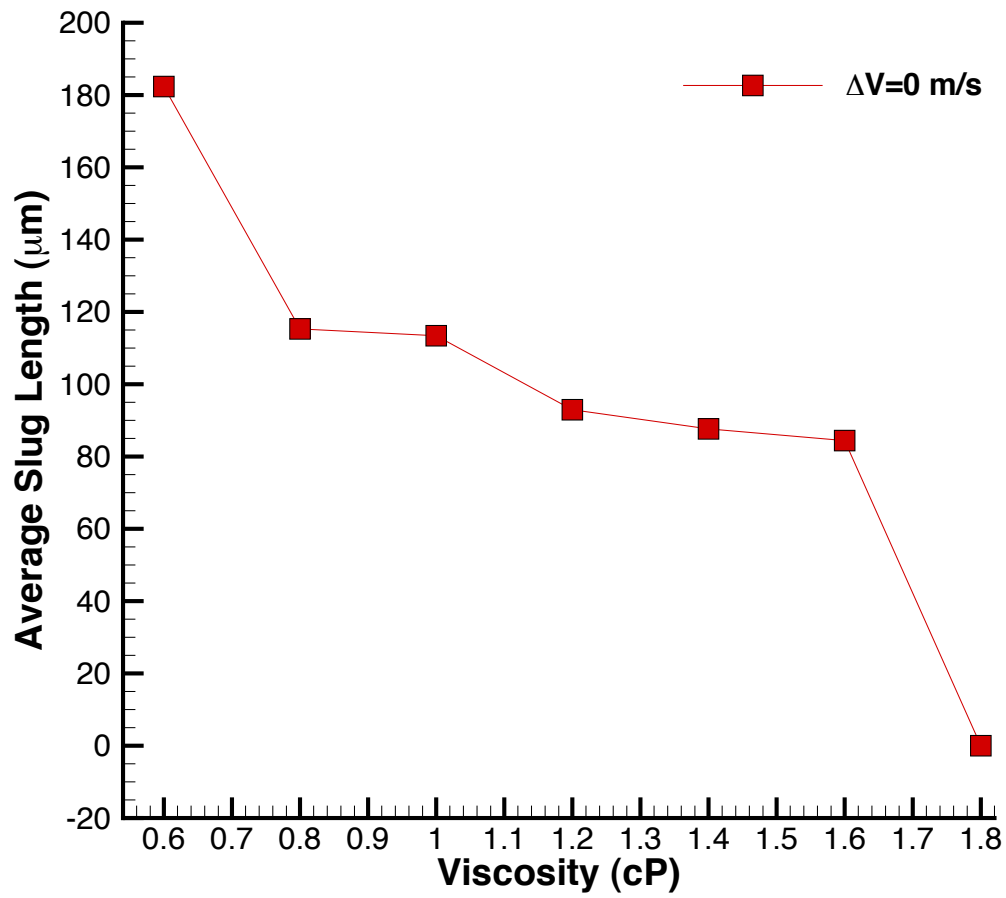


**Figure 4.10:** A plot of slug length vs. fuel viscosity for  $\Delta V = 0$ . At 1.8  $\text{cP}$ , the system transitions to annular flow, with no slugs being made.

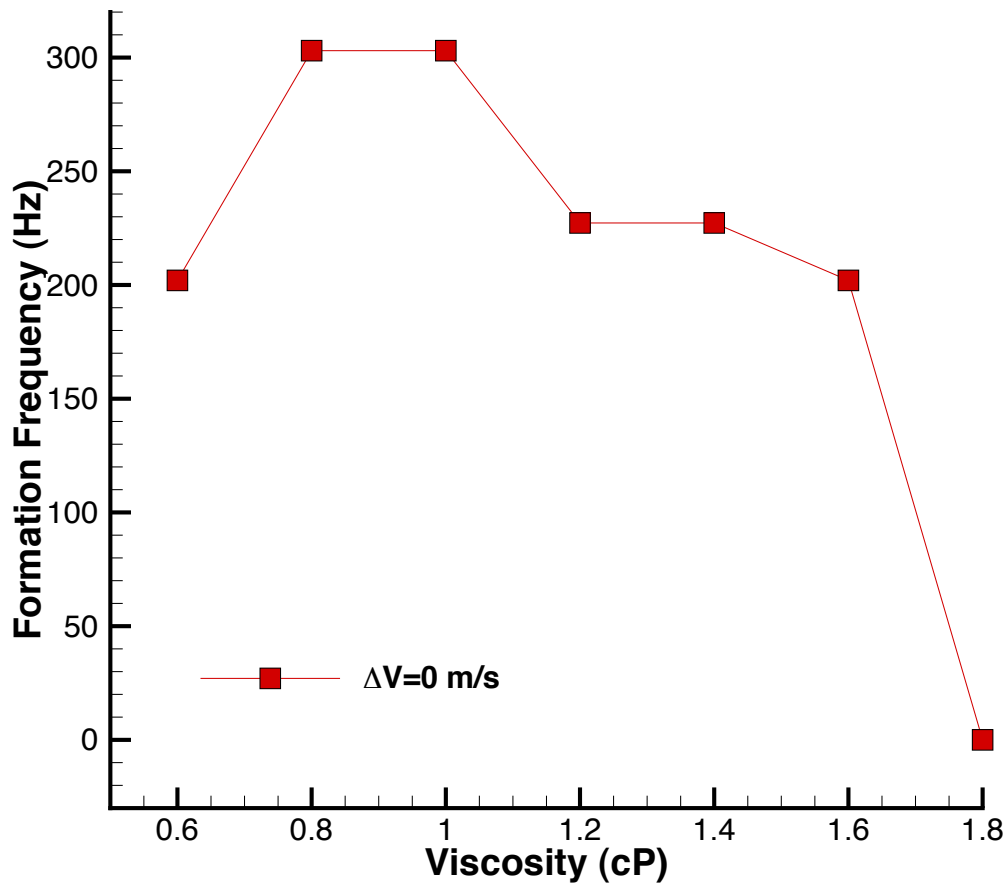


**Figure 4.11:** A plot of slug formation frequency vs. fuel viscosity for  $\Delta V = 0$ . As the system transitions to annular flow at 18 cP, the formation frequency drops to 0.

## 4.5 Effective Impulse and Thrust

The effects of the changes in slug length and formation frequency on the thrust are plotted below. For comparison, the baseline thrust of the system was calculated and plotted as well. The maximum thrust of a monopropellant thruster can be calculated

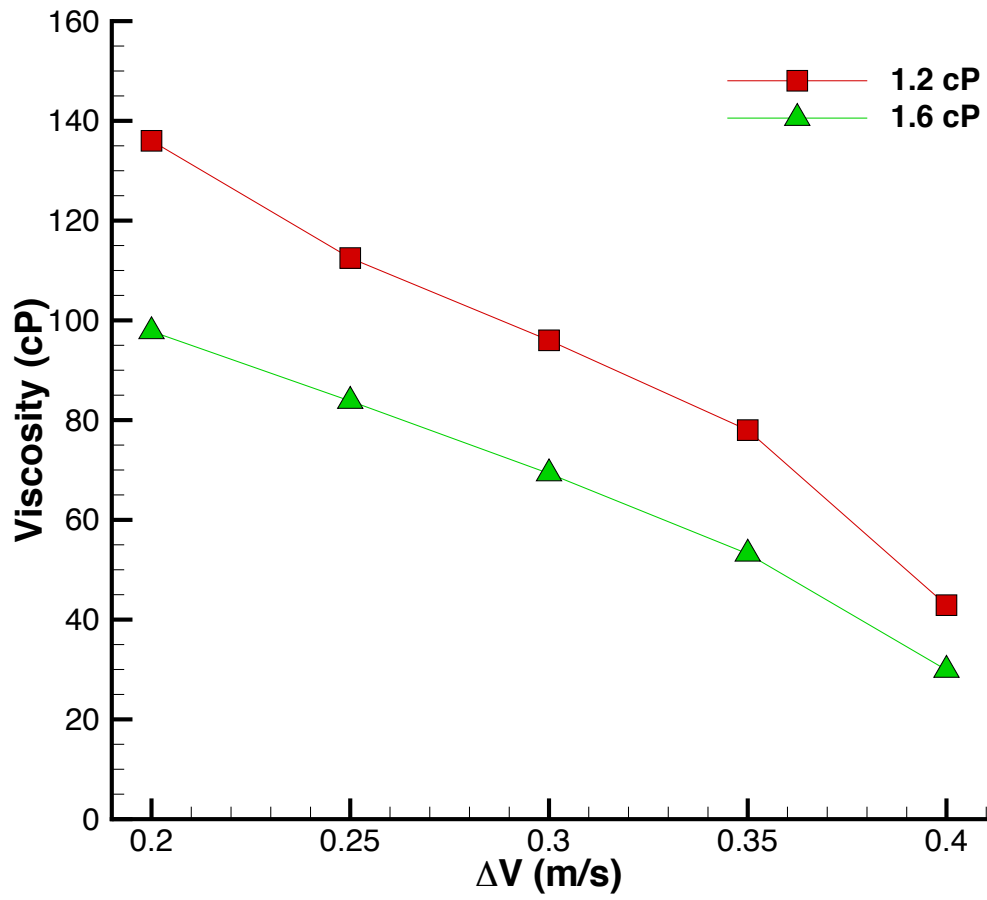


**Figure 4.12:** A plot of slug length vs.  $\Delta V$  for two different fuel viscosities. There is a clear similarity between the two solutions.

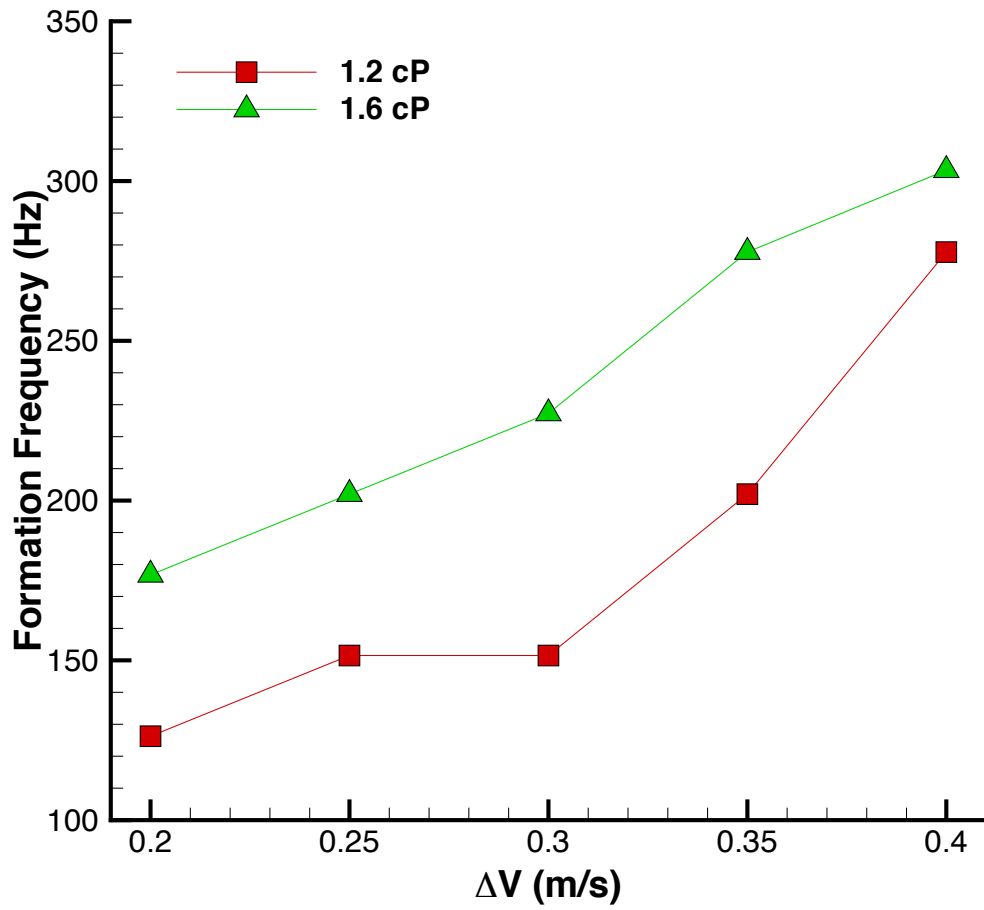


**Figure 4.13:** A plot of slug formation frequency vs.  $\Delta V$  for two different fuel viscosities. There is a clear similarity between the two solutions.

from:

$$F_t = \dot{m}I_{sp}g_0 \quad (4.1)$$

For the channel geometry and flow rates of the simulated system, this would result in a thrust of  $604 \mu N$ . The thrust levels calculated for each of the parameters of interest ranged between 45% and 70% below this baseline thrust calculation.

The impulse per slug, which is only a function of the slug length, is plotted for each of the parameters as well. In all cases, the impulse per slug is well below  $1 \mu N s$ . As the target impulse bit of the system is  $O(100 \mu N s)$ , typical operation will require the formation of several hundred of these slugs per firing.

In Section 3.1, above, it was shown that there is a transition in the system that occurs as the surface tension coefficient increases from .06 to .07 N/m, and that from .07 to .10 N/m the mass flow rate increases by only 11%. This transition can be clearly seen in Figure 4.14, as there is a 1315% increase in thrust between .06 and .07 N/m, but only an 11% increase in thrust between .07 and .10 N/m. To ensure predictable behavior of the system, the microthruster should be operated in the .07 to .10 N/m range. This would require minimizing contaminants to the system, and limiting the change in temperature of the  $H_2O_2$ .

The transition in detachment mechanism that occurs as the contact angle increases from 150 to 160 degrees, and the corresponding changes in slug length and formation frequency, manifest as a decrease in total thrust over this range. While there is a clear decrease in the thrust, as shown in Figure 4.16, the total percent decrease in thrust from the maximum (at 150 degrees) to the minimum (at 170 degrees) is only 25%. As variations in contact angle are primarily the result of contamination, preventing contaminants from entering the system could minimize the actual thrust variation during a spaceflight. Additionally, designing the microchannel to avoid the region

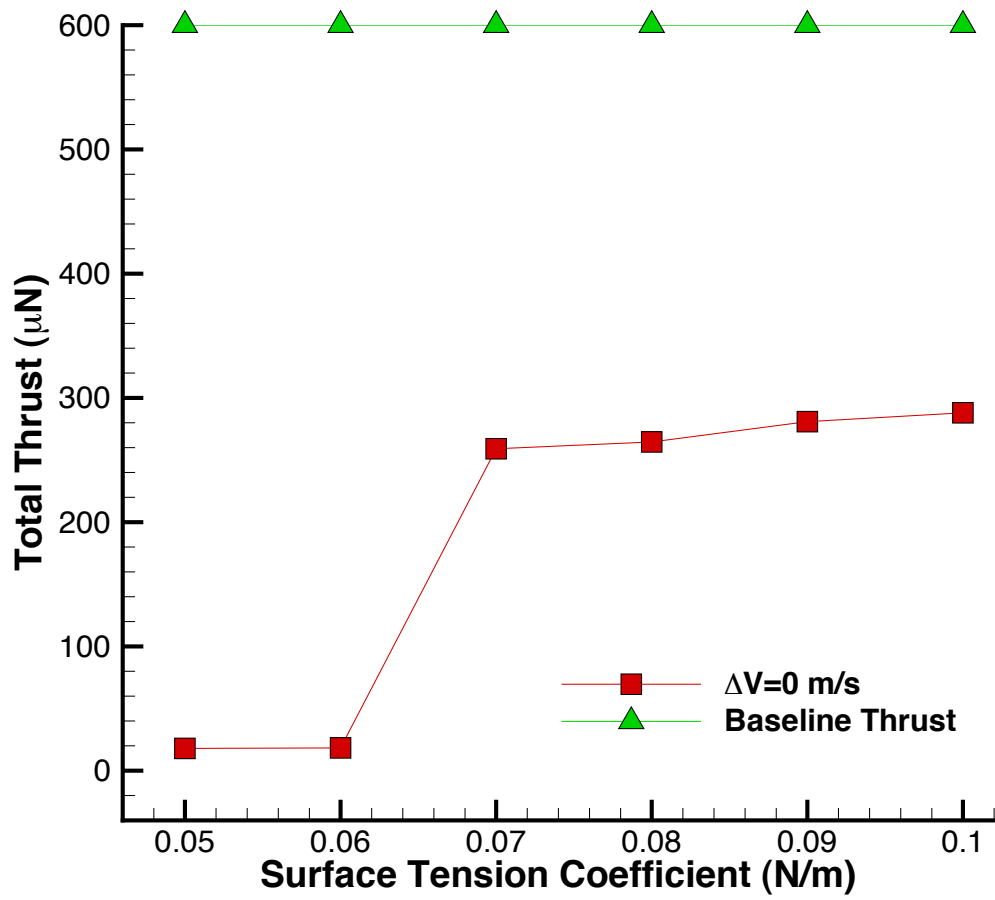


**Figure 4.14:** A plot of the total thrust vs. surface tension coefficient for  $\Delta V = 0 \frac{m}{s}$ . The baseline thrust is plotted in green.

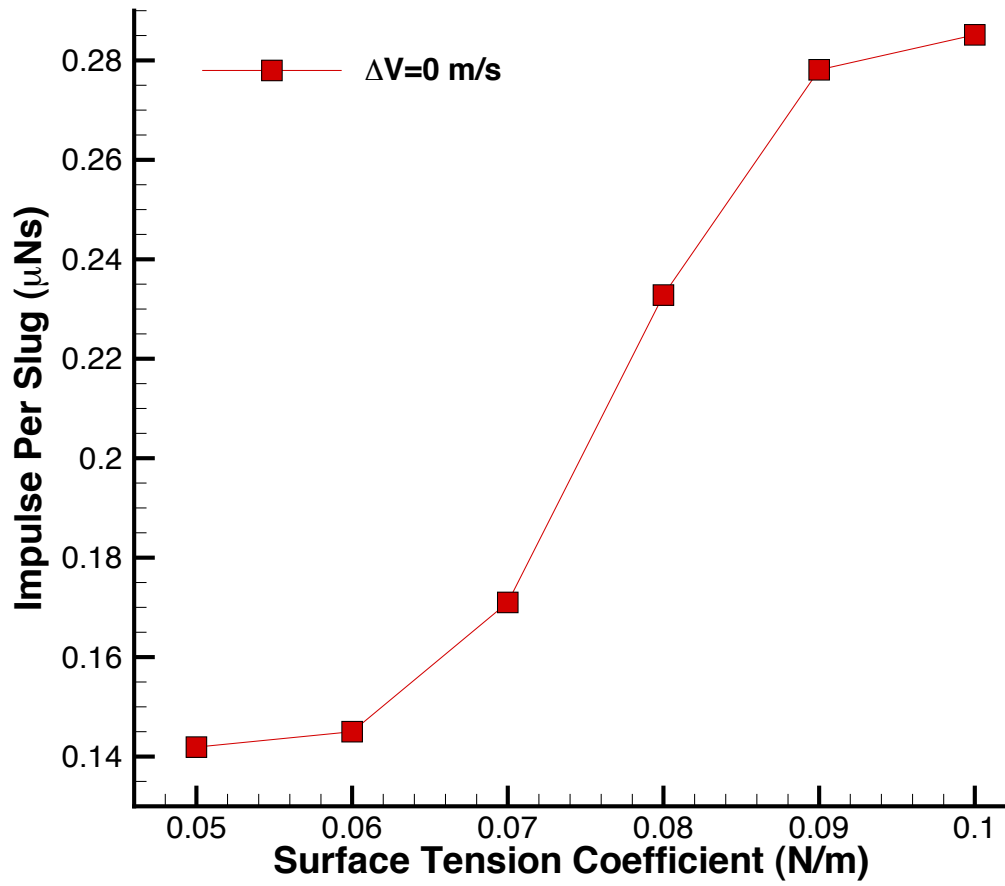


**Figure 4.15:** A plot of the impulse per slug vs. surface tension coefficient for  $\Delta V = 0 \frac{m}{s}$ .

between 150 and 160 degrees would result in more stable operation.

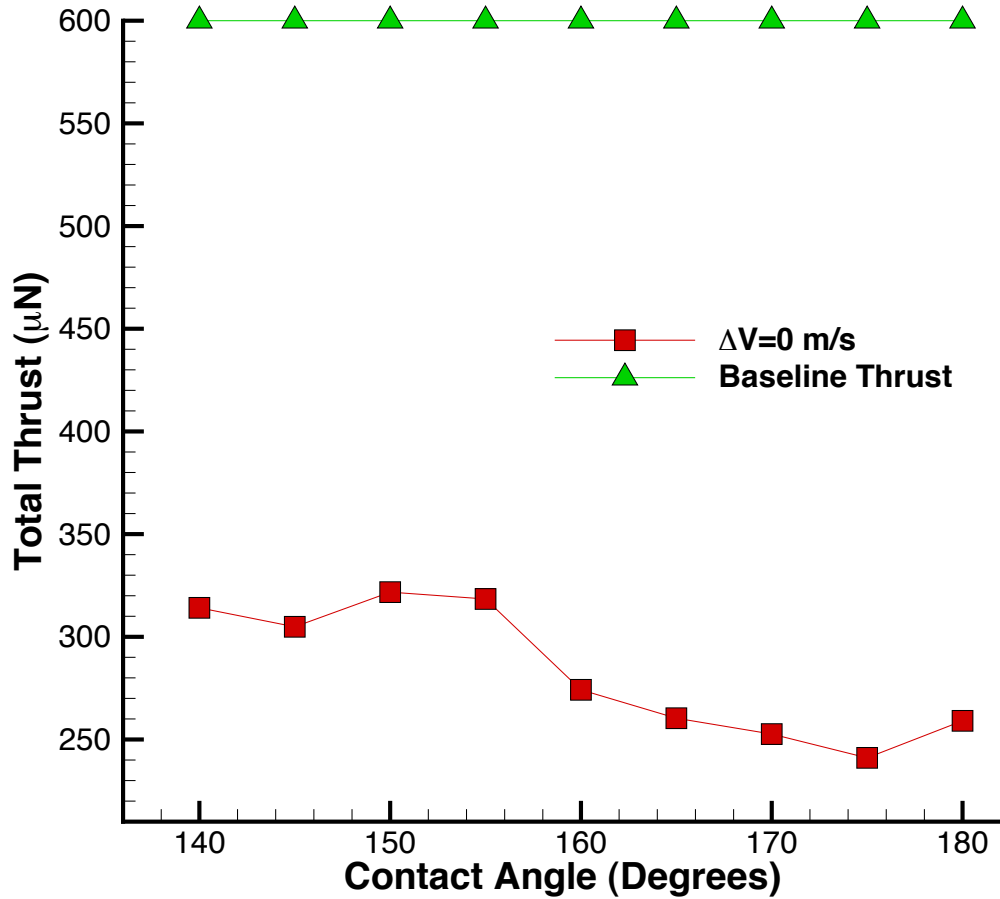


**Figure 4.16:** A plot of total thrust vs. contact angle for  $\Delta V = 0 \frac{m}{s}$ . The baseline thrust is plotted in green.

The thrust as a function of changes in viscosity, shown in Figure 4.18, shows that there are two different thrust regions that exist in the system. In the first, between .6 and 1.0 cP, the thrust starts at  $277 \mu\text{N}$  and decreases by 6%. From 1.0 to 1.2 cP, the thrust decreases by 38% to  $159 \mu\text{N}$ , then from 1.2 to 1.6 cP the thrust decreases by 19%. At 1.8 cP no slugs are produced, and thus the thrust goes to zero. This

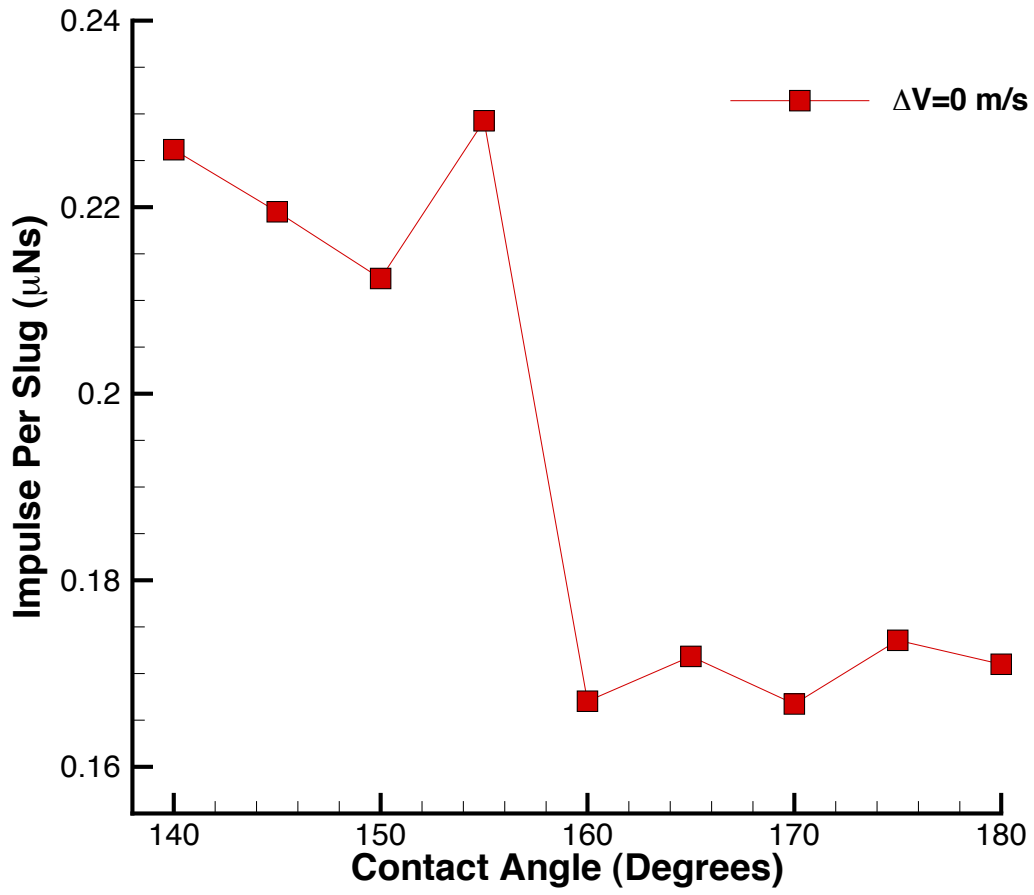
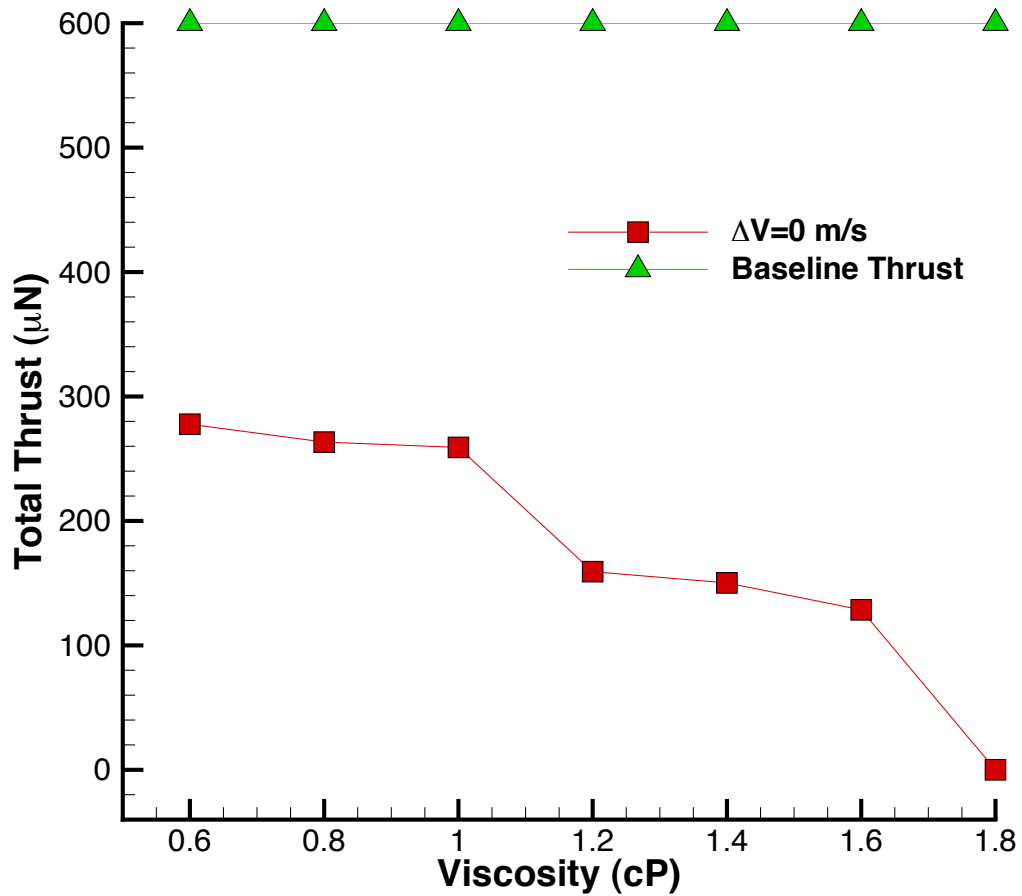


Figure 4.17: A plot of impulse per slug vs. contact angle for  $\Delta V = 0 \frac{m}{s}$ .

seems to show that there are two stable regions of operation, with the region between .6 and 1.0 cP, which corresponds to the temperature range of 50° to 25°, being the most stable. Designing the system to maintain the temperature of the  $H_2O_2$  in this range, should allow for stable operation of the system.



**Figure 4.18:** A plot of total thrust vs. viscosity for  $\Delta V = 0 \frac{m}{s}$ . The baseline thrust is plotted in green.

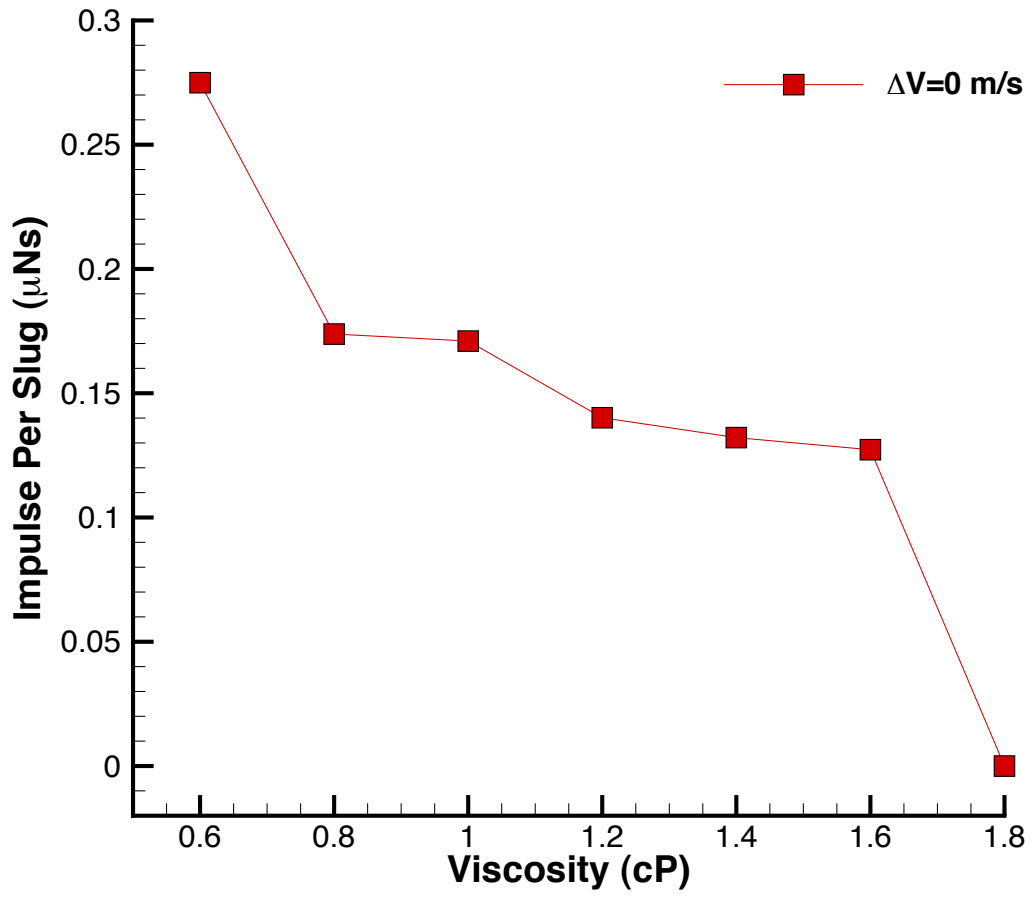


Figure 4.19: A plot of impulse per slug vs. viscosity for  $\Delta V = 0 \frac{m}{s}$ .

# Chapter 5

## Conclusions

In this study, a computational model of dispersed slug formation at a microchannel junction was developed and used to examine the sensitivity of the slug characteristics to important material properties. The envisioned application of the slug formation is that of a discrete  $H_2O_2$  monopropellant fuel injection scheme for nanosat micro-propulsion. Given the extremely low thrust and impulse levels involved, the sensitivity analysis is quite important in assessing design robustness. Specifically, the effects of variable surface tension, contact angle and fuel viscosity were examined; these variations might arise naturally under conditions of system contamination and/or thermal variations.

For each of the parameters studied, there exist regions where the small changes in the material property can cause the flow to transition from one slug formation regime to another, with a corresponding discontinuous change in slug formation characteristics. In the case of the surface tension coefficient, this transition starts at .06 N/m; above this value the slug length increases rapidly before stabilizing around .09 N/m. The contact angle influences the slug length by causing a shift in the location of the slug formation; for values less than 150 degrees the slugs are formed at the

junction, while values greater than 160 degrees result in a downstream pinch-off with smaller slugs. As the viscosity of the fuel is increased, the slug length decreases until it transitions to annular flow for values larger than 1.6 cP.

The thrust and impulse per slug were calculated using the slug length and formation frequency, and so they show similar discontinuous profiles as the parameters are varied. Outside of these transition regions, however, there are stable regions where the thrust is smooth. For surface tension, this stable region exists between .07 N/m and .10 N/m where thrust decreases by 11%. As the contact angle increases from 140 and 155 degrees, the thrust decreases by 5%. There is a region between 155 and 170 degrees where the thrust drops by 25%, and between 170 and 180 degrees, the thrust increases by 14%. The thrust as a function of viscosity exhibits two stable regions, one between .6 and 1.0 cP where there is a 6% decrease in thrust, and the second between 1.2 to 1.6 cP where there is a 19% decrease in thrust.

The sensitivity of the slug characteristics, and hence thrust and impulse production, under certain flow conditions presents an area for concern for the overall robustness of the discrete monopropellant fuel injection scheme. Yet there are also highly stable regions where the slug characteristics are essentially insensitive to property variations. It follows, therefore, that future microthruster system designs should target and incorporate these stable flow regions in their baseline operating conditions to maximize operational robustness.

## 5.1 Future Work

There are several efforts that could be undertaken to further the studies discussed in this thesis. As discussed in Chapter 3, a 2D model of the system was used to ensure the greatest number of simulations could be performed. During the course

of this work, advances in computer processing power as well as improvements in the COMSOL software have made studies of a 3D model a realistic goal. While the results of the 2D simulations compare closely with the 3D model examined, it is possible that in certain regimes, there are 3D effects that are not being captured in the current simulations. With this in mind, a fully 3D simulation of the channels would be a clear next step.

A second area of interest for future study would be using the simulations to optimize the geometry of the system. The original  $90^\circ$  junction was selected for its availability in off-the-shelf microchannels due to the ease of manufacture. As MEMS fabrication techniques have continued to improve, it is now possible to create the microchannel junction over a much wider intersection angle. Additionally, the simulations could be used to identify the miniaturization limit of the system.

# References

- [1] J. Mueller, Thruster options for microspacecraft: a review and evaluation of the state-of-the art and emerging technologies, in *Micropropulsion for Small Spacecraft - Progress in Astronautics and Aeronautics*, M. Micci and A. Ketsdever, eds., vol. 187, AIAA, Reston, Va., p. 45-137, 2000.
- [2] S. Janson, The History of Small Satellites, In H. Helvajian and S. Janson (Eds.). *Small Satellites: Past, Present and Future*. (pp. 45-87). El Segundo, CA, 2008.
- [3] J. Mueller, C. Marrese, J. Polk, EH. Yang, A. Green, V. White, D. Bame, I. Chakraborty, S. Vargo, R. Reinicke, An Overview of MEMS-based micropropulsion developments at JPL, *ACTA ASTRONAUTICA*, Vol. 52, Issue 9-12, p. 881-895, May-June 2003.
- [4] S. Marcuccio, A. Genovese, M. Andrenucci, *FEEP MICROTHRUSTER TECHNOLOGY STATUS AND POTENTIAL APPLICATIONS*, 48th International Astronautical Federation Congress, Turin, Italy, 1997.
- [5] J. Baker, P. Bender, P. Binetruy, et al, *LISA: Probing the Universe with Gravitational Waves*, Version 1.0, LISA Mission Science Office, <http://lisa.jpl.nasa.gov/news.html>, January 19, 2007.

- [6] M. Neugebauer, C. W. Snyder, Solar Plasma Experiment, *Science*, Vol. 138, No. 3545, pp. 1095 - 1097, 7 December, 1962.
- [7] R. J. Bzibziak, Sr., Miniature cold gas thrusters, AIAA-1992-3256, SAE, ASME, and ASEE, Joint Propulsion Conference and Exhibit, 28th, Nashville, TN July 6-8, 1992.
- [8] J. Mueller, W. Tang, A. Wallace, W. Li, D. Bame, I. Chakraborty and R. Lawton, Design, Analysis, and Fabrication of a Vaporizing Liquid Micro-Thruster, AIAA Paper 98-3924, 34th Joint Propulsion Conference, Cleveland, OH, July 1998.
- [9] D. L. Hitt, C. M. Zakrzewski, M. K. Thomas, MEMS-Based Satellite Micropropulsion Via Catalyzed Hydrogen Peroxide Decomposition, *Smart Mater. Struct.*, 10, 1163-1175, 2001.
- [10] R. A. W. Fleron, J. H. Hales, A MEMS Based Field Emission Electrical Propulsion System With Integrated Charge Neutralizer For Nano And Pico Spacecraft, Proceedings of the 4th International Spacecraft Propulsion Conference (ESA SP-555), Cagliari, Italy, 2-9 June, 2004.
- [11] C. Scharlemann, M. Tajmar, Development of Propulsion Means For Microsatellites, AIAA-2007-5184, 43rd AIAA/ASME/SAE/ASEE Joint Propulsion Conference and Exhibit, Cincinnati, OH, July 2007
- [12] J. Nabity, G. Mason, J. Engel, J. Daily, R. Laumbay, D. Kassoy, Studies of MEMS Colloid Thrusters, AIAA-2006-5007, 42nd AIAA/ASME/SAE/ASEE Joint Prop. Conf. and Exhibit, Sacramento, CA, July 9-12, 2006.

- [13] J. Xiong, Z. Zhou, D. Sun, X. Ye, Development of a MEMS based colloid thruster with sandwich structure, *Sensors & Actuators A*, Vol. 117, Issue 1, pp. 168-172, January 2005.
- [14] D. Lewis, Jr., S. Janson, R. Cohen, Digital MicroPropulsion,, 12th IEEE International Conference on Micro Electro Mechanical Systems, pp. 517-52, 1999.
- [15] P. Fuqua, S.W. Janson, W. Hansen, H.Helvajian, Fabrication of true 3D microstructures in glass/ceramic materials by pulsed UV laser volumetric exposure techniques, *Proc. SPIE*, p 213, 1999.
- [16] R. Bayt, Analysis, Fabrication and Testing of a MEMS-based Micropropulsion System, FDRL TR 99-1, Ph.D. Thesis supervised by Prof. Kenneth Breuer, M.I.T. Dept. of Aeronautics and Astronautics, June, 1999.
- [17] J. Blandino, M. McDevitt, J. Mueller, D. Bame, & A. Green. Characterization of dryout point in the vaporizing liquid microthruster. *Journal of Propulsion and Power*, 22(3), 677683, 2006.
- [18] J. Mueller. Review and Applicability Assessment of MEMS-Based Microvalve Technologies for Microspacecraft Propulsion, *Micropropulsion for Small Spacecraft*, Progress in Astronautics and Aeronautics, Vol. 187, edited by M. Micci and A. Ketsdever, AIAA, Reston, VA, pp. 449-476, 2000.
- [19] K. W. Oh, C. H. Ahn, A review of microvalves, *J. of Micromech. and Microeng.*, 16, R13-R39, 2006.
- [20] J. McCabe & D. Hitt, Monopropellant fuel injection using two-phase micro-slug formation. *Proceedings of 39th Annual AIAA Fluid Dynamics Conference*, 2009.

- [21] T.R. Harris, D.L. Hitt, and R.G. Jenkins, Discrete Micro-Slug Formation for Micro-Thruster Propellant Delivery, AIAA Paper 2005-0676, 2005.
- [22] T. Cubaud and C. Ho, Transport of bubbles in square microchannels, *Physics of Fluids*, Volume 16, No 12, pp. 4575-85, 2004.
- [23] T. Cubaud, M. Tatineni, X. Zhong, and C. M. Ho, Bubble dispenser in microfluidic devices, *Phys. Review E*, 72, 037302, 2005.
- [24] J.W. McCabe, Monopropellant Fuel Injection Using Two-Phase Micro-Slug Formation. (Master's Thesis) University of Vermont, Burlington, VT, 2009.
- [25] J. Sethian. Level set methods and fast marching methods: evolving interfaces in computational geometry, fluid mechanics, computer vision, and materials science, 1999.
- [26] A.K. Tornberg, B. Enhquist, A finite element based level set method for multi-phase flow applications, *Comput. Visual. Sci.* 3, 93-101, 2000.
- [27] E. Olsson & G. Kreiss, A conservative level set method for two phase flow. *Journal of Computational Physics*, 2005.
- [28] E. Olsson & G. Kreiss, A conservative level set method for two phase flow II. *Journal of Computational Physics*, 2007.
- [29] N.A. Mortensen, F. Okkels, H. Bruus, Reexamination of Hagen-Poiseuille flow: Shape dependence of the hydraulic resistance in microchannels, *Phys. Rev. E*, 71, 057301, 2005.
- [30] D. Qian & A. Lawal. Numerical study on gas and liquid slugs for Taylor flow in a T-junction. *Chemical Engineering Science*, 2006.

- [31] T. Cubaud & T. Mason, Capillary threads and viscous droplets in square microchannels. *Physics of Fluids*, 2008.

# Appendix A

**Listing A.1:** MATLAB Script used to calculate slug length and formation frequency

```
clear all; close all;
format short
FrameRate = 20000;
MaxRow = 466;
5 MinRow = 442;
MaxCol = 1551;
MinCol = 417;

MinFrame = [5,5,5,5,5,5];
10 MaxFrame = [36,37,41,43,45];
FileRange = {'V1', 'V2', 'V3', 'V4', 'V5'};

15 for q = 1:size(FileRange,2)
    ImageData = 0;

    cd(FileRange{q});
```

20

```
FrameName = ['00' num2str(MaxFrame(q)) '.jpg'];  
ImageData = imread(FrameName);  
[ nrow ncol ndim ] = size(ImageData);
```

25

```
ImageData = ImageData(MinRow:MaxRow,MinCol:MaxCol,:);  
ImageData = rgb2gray(ImageData);  
%background = imopen(ImageData,strel('disk',15));  
%ImageData = ImageData - background;
```

30

```
%ImageData = imadjust(ImageData);  
level = graythresh(ImageData);  
bw = im2bw(ImageData,level);  
bw = bwareaopen(bw, 50);  
%figure, imshow(bw)
```

35

```
cc = bwconncomp(bw, 4);  
cc.NumObjects;  
BubbleData = regionprops(cc, 'Area','MajorAxisLength');
```

40

```
for BubbleNumber = 1:cc.NumObjects  
    AreaData(BubbleNumber)=BubbleData(BubbleNumber)...  
        Area;  
    LengthData(BubbleNumber)=BubbleData...  
        (BubbleNumber).MajorAxisLength
```

```
end
```

45

```

%   for ct = 2:length(BubbleData)
%       BubbleL(ct-1) = BubbleData(ct).MajorAxisLength;
%       BubbleA(ct-1) = BubbleData(ct).Area;
50 %   end

PixData = ImageData(:,:,1);

% Perform averaging over row data
% and eliminate DC component
PixData = mean(PixData,1);
PixData = double( double(PixData) - mean(PixData));

60 % Plot the pixel intensity data
% figure;
% plot(PixData);

% Compute and plot power spectrum
% for intensity sequence
65 %

NPixData = length(PixData);
MyFFT= fft(PixData); % compute FFT

70 % compute power spectral density
MyPow = MyFFT.*conj(MyFFT);
% normalize spectral data

```

```

MyPow = MyPow/max(MyPow);

75
freqrange = linspace(0,0.5,round(NPixData/2))...
           *FrameRate;

% figure;
80 % semilogx(freqrange,MyPow(1:NPixData/2));
% xlabel('Frequency(Hz)')
% ylabel('Normalized Spectral Density')

AveArea=mean(sum(AreaData)./sum(AreaData~=0));
85 AveLength=mean(sum(LengthData)./sum(LengthData~=0));

[maxA,ind] = max(MyPow(:));
[m] = ind2sub(size(MyPow),ind);

90 FrequencyData(q)=freqrange(m);

cd /Users/RM/Documents/MATLAB/NanoSat;
TotalAveArea(q) = AveArea*(3.5714)^2;
TotalAveLength(q) = AveLength*3.5714;
95 TotalThrust(q) = TotalAveArea(q)*10^-12*...
   FrequencyData(q)*998*9.81*154;

end

data = [(0:.05:.2)', TotalAveArea'];

```

```

100 [nrows, ncols] = size(data);

fp = fopen('area.plt','w'); % open the data file

105 fprintf(fp,'TITLE="%s" \n', 'Average Area');
fprintf(fp,'VARIABLES="%s",...
        "%s" \n', 'Delta V', 'Average Area');
fprintf(fp,'ZONE F=POINT I= %d\n', nrows);
fprintf(fp,'T=%s\n', 'History');

110 for i=1:nrows
        fprintf(fp,'%f %f\n', data(i,1), data(i,2));
end

115 fclose(fp);

data = [(-.2:.05:0)', flipdim(FrequencyData,2)'];

[nrows, ncols] = size(data);

120 fp = fopen('frequency.plt','w'); % open the data file

fprintf(fp,'TITLE="%s" \n', 'Formation Frequency');
fprintf(fp,'VARIABLES="%s", "%s" \n',...
125         'Delta V', 'Formation Frequency');
fprintf(fp,'ZONE F=POINT I= %d\n', nrows);

```

```

fprintf(fp, 'T=%s\n', 'History');

for i=1:nrows
130     fprintf(fp, '%f %f\n', data(i,1), data(i,2));
end

fclose(fp);

135 data = [(-.2:.05:0)', flipdim(TotalAveLength,2)'];

[nrows, ncols] = size(data);

fp = fopen('length.plt', 'w'); % open the data file
140

fprintf(fp, 'TITLE="%s" \n', 'Average Length');
fprintf(fp, 'VARIABLES="%s", "%s" \n', ...
        'Delta V', 'Average Length');
fprintf(fp, 'ZONE F=POINT I= %d\n', nrows);
145 fprintf(fp, 'T=%s\n', 'History');

for i=1:nrows
    fprintf(fp, '%f %f\n', data(i,1), data(i,2));
end
150

fclose(fp);

data = [(0:.05:.2)', TotalThrust'];

```

```

155 [nrows, ncols] = size(data);

fp = fopen('thrust.plt','w'); % open the data file

fprintf(fp, 'TITLE="%s" \n', 'Total Thrust');
160 fprintf(fp, 'VARIABLES="%s", "%s" \n', ...
           'Delta V', 'Total Thrust');
fprintf(fp, 'ZONE F=POINT I= %d\n', nrows);
fprintf(fp, 'T=%s\n', 'History');

165 for i=1:nrows
    fprintf(fp, '%f %f\n', data(i,1), data(i,2));
end

fclose(fp);

```